REPORT DOCUMENTATION PAGE

1. REPORT DATE (DD-MM-YYYY)	2. REPORT TYPE	3. DATES COVERED (From - To)
10-03-2008	Journal Article	

4. TITLE AND SUBTITLE

Deriving Sea Surface Salinity & Density Variations from Microwave Radiometer Measurements: Applications to Coastal Plumes Using STARRS

5a. CONTRACT NUMBER

5b. GRANT NUMBER

5c. PROGRAM ELEMENT NUMBER
0602435N

6. AUTHOR(S)

Derek M. Burrage, Joel C. Wesson, Jerry Miller

5d. PROJECT NUMBER

5e. TASK NUMBER

5f. WORK UNIT NUMBER
73-6629-06-5

7. PERFORMING ORGANIZATION NAME(S) AND ADDRESS(ES)

Naval Research Laboratory
Oceanography Division
Stennis Space Center, MS 39529-5004

8. PERFORMING ORGANIZATION REPORT NUMBER
NRL/JA/7330--07-7162

9. SPONSORING/MONITORING AGENCY NAME(S) AND ADDRESS(ES)

Office of Naval Research
800 N. Quincy St.
Arlington, VA 22217-5660

10. SPONSOR/MONITOR'S ACRONYM(S)
ONR

11. SPONSOR/MONITOR'S REPORT NUMBER(S)

12. DISTRIBUTION/AVAILABILITY STATEMENT

Approved for public release, distribution is unlimited.

20080409006

13. SUPPLEMENTARY NOTES

14. ABSTRACT

Using brightness temperature Tb measurements from L-band airborne microwave radiometers, with independent sea surface temperature (SST) observations, sea surface salinity (SSS) can be remotely determined with errors of about 1 psu in temperate regions. Nonlinearities in the relationship between Tb, SSS, and SST produce variations in the sensitivity of salinity S to variations in Tb and SST. Despite significant efforts devoted to SSS remote sensing retrieval algorithms, little consideration has been given to deriving density D from remotely sensed SSS and SST. Density is related to S and T through the equation of state. It affects the ocean's static stability and its dynamical response to forcings. By chaining together two empirical relationships (flat-sea emissivity and equation of state) to form an inversion algorithm for sea surface density (SSD) in terms of Tb and SST, we develop a simple L-band SSD retrieval algorithm. We use this to investigate the sensitivity of SSD retrievals to observed Tb and SST and infer errors in D for typical sampling configurations of the airborne Salinity, Temperature, And Roughness Remote Scanner (STARRS) and satellite-borne Soil Moisture and Ocean Salinity (SMOS) and Aquarius radiometers. We then derive D from observations of river plumes obtained using STARRS and demonstrate several oceanographic applications: the observations are used to study varia- tions in T and S effects on D in the Mississippi plume, and the across-shelf density gradient is used to infer surface geostrophic shear and subsurface geostrophic current in the Plata plume. Future basin-scale applications of SSD retrievals from satellite-borne microwave radiometers such as SMOS and Aquarius are anticipated.

15. SUBJECT TERMS

Aquarius, Salinity, Temperature, And Roughness Remote Scanner (STARRS), Soil Moisture and Ocean Salinity (SMOS)

16. SECURITY CLASSIFICATION OF:			17. LIMITATION OF ABSTRACT	18. NUMBER OF PAGES	19a. NAME OF RESPONSIBLE PERSON
a. REPORT	b. ABSTRACT	c. THIS PAGE	UL	21	Derek Burrage
Unclassified	Unclassified	Unclassified			19b. TELEPHONE NUMBER (Include area code) 228-688-5241

Deriving Sea Surface Salinity and Density Variations From Satellite and Aircraft Microwave Radiometer Measurements: Application to Coastal Plumes Using STARRS

Derek Burrage, Joel Wesson, and Jerry Miller

Abstract—Using brightness temperature Tb measurements from L-band airborne microwave radiometers, with independent sea surface temperature (SST) observations, sea surface salinity (SSS) can be remotely determined with errors of about 1 psu in temperate regions. Nonlinearities in the relationship between Tb, SSS, and SST produce variations in the sensitivity of salinity S to variations in Tb and SST. Despite significant efforts devoted to SSS remote sensing retrieval algorithms, little consideration has been given to deriving density D from remotely sensed SSS and SST. Density is related to S and T through the equation of state. It affects the ocean's static stability and its dynamical response to forcings. By chaining together two empirical relationships (flat-sea emissivity and equation of state) to form an inversion algorithm for sea surface density (SSD) in terms of Tb and SST, we develop a simple L-band SSD retrieval algorithm. We use this to investigate the sensitivity of SSD retrievals to observed Tb and SST and infer errors in D for typical sampling configurations of the airborne Salinity, Temperature, And Roughness Remote Scanner (STARRS) and satellite-borne Soil Moisture and Ocean Salinity (SMOS) and Aquarius radiometers. We then derive D from observations of river plumes obtained using STARRS and demonstrate several oceanographic applications: the observations are used to study variations in T and S effects on D in the Mississippi plume, and the across-shelf density gradient is used to infer surface geostrophic shear and subsurface geostrophic current in the Plata plume. Future basin-scale applications of SSD retrievals from satellite-borne microwave radiometers such as SMOS and Aquarius are anticipated.

Index Terms—Aquarius, brightness temperature, coastal plumes, density, emissivity, microwave radiometry, retrieval algorithm, Salinity, Temperature, And Roughness Remote Scanner (STARRS), sea surface salinity (SSS), Soil Moisture and Ocean Salinity (SMOS).

I. INTRODUCTION

R ECENT advances in microwave remote sensing enable precise measurements of the brightness temperature (Tb) of seawater at L-band ($\sim$1.4 GHz) to be obtained over coastal regions from a light aircraft [1], [2], whereas the Soil Moisture and Ocean Salinity (SMOS) and Aquarius satellite missions to be launched in the near future will provide a similar capability over the deep global oceans [3]–[6]. Modern airborne L-band microwave radiometers are sensitive enough to detect Tb variations at better than 0.5-K precision under operational conditions, at typical spatial resolutions of 1 km, whereas satellite-borne systems are being designed to provide effective 0.1-K precision, after data averaging, on spatial scales of about 100–300 km.

The brightness temperature at the surface Tb is proportional to the sea surface temperature (SST) and the emissivity. The emissivity is itself a function of SST and conductivity (which together determine the salinity), roughness (primarily determined by wind speed), beam incidence angle θ, and antenna polarization p. The relationship between Tb and sea surface salinity (SSS), SST, θ, and p for a flat calm sea may be obtained from the so-called "flat sea" empirical emissivity model relationships, e.g., [7] and [8], and various semianalytical or empirical relationships to account for the roughness influence are available [9], [10]. By taking into account reflected sources of radiation, both atmospheric and extraterrestrial (galactic, cosmic background, and solar), as well as atmospheric absorption effects, it is possible to edit or correct the Tb values and, together with SST, invert them to estimate SSS. Based on the Klein and Swift relation [7], a precision of 0.5 K corresponds to a retrieved SSS precision of 1 psu (for single-point measurements under temperature conditions typically encountered in mid- and low-latitude coastal seas).

Significant effort has been expended to date to define and refine the algorithms for SSS retrieval from L-band Tb, taking into account the aforementioned factors. However, the possibility of deriving sea surface density (SSD) indirectly from retrieved SSS and SST data or directly from the SST and Tb remote sensing measurements has received little consideration. This is so, despite the fundamental importance of density in governing ocean wave and circulation dynamics, including baroclinic currents and shear instabilities, convective overturn,

D. Burrage and J. Wesson are with the Ocean Sciences Branch, Naval Research Laboratory, Stennis Space Center, MS 39529 USA (e-mail: burrage@nrlssc.navy.mil).

J. Miller was with the Ocean Sciences Branch, Naval Research Laboratory, Stennis Space Center, MS 39529 USA. He is now with the Consortium for Oceanographic Research and Education, Washington, DC 20005 USA.

Color versions of one or more of the figures in this paper are available online at http://ieeexplore.ieee.org.

Digital Object Identifier 10.1109/TGRS.2007.915404

and various air–sea interaction processes. Both the seawater equation of state (SES), which determines D as a function of S, T, and pressure P [11], and the equations governing flat-sea emissivity [7], which determine Tb from SST, SSS, θ, and p are, in general, nonlinear. As demonstrated here, the sensitivity of SST, SSS, and SSD to Tb significantly changes throughout the range of brightness temperatures typically encountered over the coastal ocean. In the text, we use the acronyms SST, SSS, and SSD to denote the sea surface temperature, salinity, and density, respectively. The corresponding mathematical or graphic symbols are T (or Ts, to emphasize the surface value and distinguish it from brightness temperature Tb), S, and D, where surface values are understood, except where T, S, or D are implicit or explicit functions of depth, as in $T(z)$, $S(z)$, or $D(z)$. Similarly, $P(z)$ denotes the pressure at depth z in the ocean, unless $z = 0$, in which case it refers to surface (atmospheric) pressure. The radiometers actually measure brightness temperature Ta at the antenna, but radiometer data processing algorithms transform this to its surface value Tb by applying various environmental corrections based on a radiative transfer model.

We formulate a retrieval algorithm for SSD using the available empirical functions for the equation of state and flat-sea emissivity. Accounting for the controlling influence of antenna incidence angle and polarization, we then compute the sensitivity of the derived SSD to SST and SSS. This allows the SSD error for particular SST and Tb input error levels to be determined via the emissivity model and the SES.

At first order, observed Tb varies directly with respect to SST and inversely with respect to SSS, whereas SSD varies inversely with respect to SST and directly with respect to SSS. This implies an inverse relation between Tb and D that is simultaneously determined by S and Ts. These relationships may affect the detection of surface density fronts. Considering a specific example, compensating effects on D of variations in S and T are sometimes observed across upward-sloping coastal fronts where warm saline ocean water outcrops above and seaward of cooler and fresher coastal water [12]. In this density-compensating situation, both SSD and Tb variations across the outcropping front will be small, and the front will be better located using SST and SSS retrievals. In the opposite situation, where S and T reinforce each other in their effect on D, both Tb and SSD may vary strongly, but inversely, across the front, which consequently may be more reliably detected using SSD retrieval. In general, the errors associated with the retrieval of SSD and SSS from Tb may be compensating or reinforcing to a lesser or greater extent, depending on the water mass locations in the T–S parameter space. As demonstrated here, a simple vector index, based on the T- and S-dependent density ratio [13], can be employed to determine which of SSS and SST dominates the SSD variations and whether the resulting T and S fields are significant in either compensating or reinforcing the density variation.

We have applied the algorithms for computing SSD to measurements from the Salinity, Temperature, And Roughness Remote Scanner (STARRS) of the Naval Research Laboratory (NRL) (see Section V and Appendix A for a detailed description of the instrument). The measurements were obtained during separate surveys of the Mississippi River plume (in the northern Gulf of Mexico) and the La Plata River plume (off the South American Atlantic Coast). Both plumes were surveyed in summer and winter. A variety of conditions illustrate how the sensitivity of SSS and SSD retrievals to observational errors varies and reveal the potential benefits of deriving SSD from microwave L-band data in remote sensing studies of coastal river plumes.

This paper has several innovative features. To our knowledge, this is the first time that SSD has been derived from remote L-band microwave radiometer observations. Similarly, the exploration of the combined parameter space of the equation of state and the L-band emissivity model and the presentation of graphs illustrating the sensitivity of SSD to variations and errors in SST, SSS, and Tb are novel. Furthermore, surface geostrophic currents have previously been determined directly from radar altimeter measurements of sea surface height (SSH) by various investigators (e.g., [14] and [15], based on the geostrophy theory; and [16], combining geostrophic with Ekman theory using auxiliary wind data) and indirectly from thermal infrared (IR) and microwave SST measurements (e.g., [17], based on the quasi-geostrophic (QG) theory). However, the derivation of near-surface geostrophic shear and subsurface geostrophic currents from a combination of remotely sensed SSS and SST data and thermal wind equations (through appropriate assumptions), has not previously been demonstrated. Finally, a simple extension of the Turner angle [18], [19] is proposed to give a vector representation of both horizontal density compensation and the combined strength of the associated T and S gradients.

In the remainder of this paper, we examine the relationships determining SSD from Tb and SST, develop the SSD algorithm, and investigate SSD sensitivity to SST and Tb errors (Section II). We then consider how density varies and introduce the density compensation index, i.e., the "Turner vector" (Section III). The results are used to study horizontal surface density gradients and to develop a method to infer near-surface currents (Section IV). We proceed to describe relevant field results and demonstrate the application of these techniques (Section V). Finally, we discuss the algorithm and possible enhancements, evaluate the results (Section VI), and draw conclusions (Section VII). Details of the field survey instrumentation and logistics and mathematical derivations are provided in the Appendixes.

II. DERIVING SSD

A. Density Retrieval Algorithm

The empirical Klein and Swift algorithm (KS77) [7], based on the Debye model of the dielectric constant [20], is commonly used to determine the brightness temperature Tb of a calm ("flat") sea surface, given its physical temperature Ts and salinity S [Fig. 1(a)]. The brightness temperatures (vertical axis) are for vertically polarized (V-Pol) signals, at a representative incidence angle of $22°$, that were chosen to coincide with the intermediate right and left beams of the STARRS L-band radiometer that we used for algorithm validation (see Section V

(a)

Density =[1000:5:1030] kg m⁻³, Salinity=[0:5:40] psu

(b)

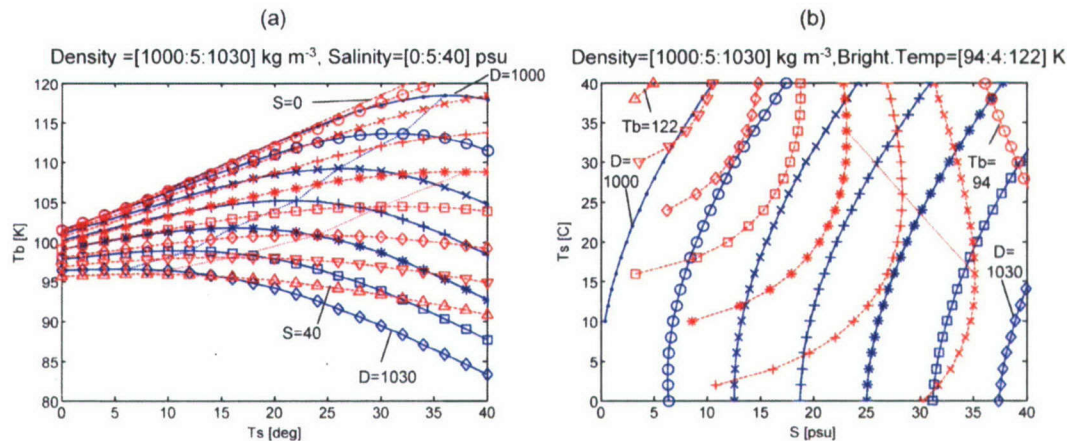Density=[1000:5:1030] kg m⁻³,Bright.Temp=[94:4:122] K

Fig. 1.   Nonlinear empirical functions determining salinity S and density D from L-band brightness temperature Tb and physical surface temperature Ts at an incidence angle of $22°$. (a) Flat-sea emissivity (KS77) showing S (red or gray, dashed) and D (blue or black, solid) versus Tb and Ts. (b) Equation of state showing D (blue or black, solid) and Tb (red or gray, dashed) versus Ts and S. Ranges and corresponding increments, in the format [low:incr:high] for S, D, and Tb, appear at the top, and the low and high contour lines are labeled. The dotted lines trace relevant turning points.

and Appendix A-1 for instrument specifications). For the V-Pol signals, the brightness temperatures for a given Ts and S are progressively higher at higher incidence angles, but the choice of incidence angle does not otherwise change the qualitative features mentioned here. For horizontally polarized (H-Pol) signals, the brightness temperatures are the same as those for V-Pol at nadir but are progressively lower at higher incidence angles. The pattern of variation of S for H-Pol is otherwise quite similar to that for V-Pol. The KS77 algorithm, as originally defined, has a validity range of 4–35 psu in S, 0 °C to 30 °C in T, and 0° to 90° in θ, and it applies to radiation at frequencies lower than the X-band (including, in particular, the L- and C-band, which are detected by our microwave instrumentation). Since our experience shows that it produces plausible results for S down to 0 and up to at least 40 psu, we have chosen to plot values for this extended range. When used as a salinity retrieval algorithm, the KS77 relationship is usually numerically inverted to determine S as a function of Tb and Ts.

For a given emissivity, Tb linearly varies in proportion to Ts. However, Ts (with S) influences the emissivity itself, which (for both V- and H-Pol signals) is reduced at higher Ts. Consequently, for salinities higher than about 15 psu, Tb first increases then decreases as a function of Ts, which makes Ts multivalued with respect to Tb [a line parallel to the Ts-axis intersects an isohaline at two separate values of Ts, Fig. 1(a)]. The dashed red curve identifies the maximum Tb for a given Ts. In contrast, S varies uniquely and approximately inversely (but nonlinearly) as a function of Tb, given Ts. Hence, given Ts and an observed Tb, S can be uniquely determined.

The SES (plotted in Fig. 1(b) on axes forming an oceanographer's $T-S$ diagram) uniquely determines density D as a nonlinear empirical function of Ts and S. Consequently, if Ts and S are known, D can be determined. Since S can be determined from Tb and Ts through KS77, the two relationships can be chained together to retrieve D, given Tb and Ts. Hence, D may be plotted along with S in the $Tb–Ts$ space. Here, density, which, in the oceanographic literature, is often expressed in units of Sigma-t (σ_t, the density anomaly relative to

1000 kg · m⁻³, e.g., 10 σ_t corresponds to 1010 kg · m⁻³) is computed as a function of temperature and pressure, in this case at the surface.

The density shown in relation to Tb and Ts [Fig. 1(a) (blue)] varies like S, in approximately inverse proportion to Tb. It has a similar but more pronounced pattern than S (red) with stronger negative slopes, i.e., Ts is multivalued with respect to D (a line parallel to the Ts-axis intersects an isopycnal at two separate values of Ts) and reaches a maximum (dashed blue line) at various Ts values throughout its range (1000–1030 kg · m⁻³). For retrieving S and D, near their respective turning points (local maxima), the algorithms are relatively insensitive to errors in Ts. This region of low sensitivity appears at a progressively higher Ts for density and salinity but at a lower Ts for D than for S (the red and blue dashed curves are offset, with respect to Ts).

The error sensitivity of S and D is explored in more detail in the next section, but we can immediately conclude that, in the presence of Ts errors, D exhibits low sensitivity to Ts at lower temperatures than S and that, for both S and D, the region of low sensitivity appears at progressively lower temperatures as they increase in value. The sensitivity to Ts errors is thus lower for S in relatively fresh ($S \sim 25$ psu) tropical ($Ts \sim 30$ °C) waters and in relatively saline ($S \sim 35$ psu) cool temperate ($Ts \sim 15$ °C) waters. For density, the corresponding areas of low Ts sensitivity occur either in fresher water ($S \sim 15$ psu) or at lower temperatures ($Ts \sim 23$ °C) with respect to tropical waters, whereas the differences are less pronounced in cooler waters (where the S and D maxima tend to converge).

Given the unique relationship between Tb and S or D, we can regard Tb (for a specified incidence angle θ) as being uniquely determined by the equation of state [Fig. 1(b)]. However, unlike D, which monotonically increases as S increases and Ts decreases, Tb decreases in this direction, and Ts is multivalued with respect to Tb, on the more saline side of the diagram ($S > 20$ psu); a line parallel to the vertical Ts-axis intersects a (red) Tb isoline at two separate values of Ts.

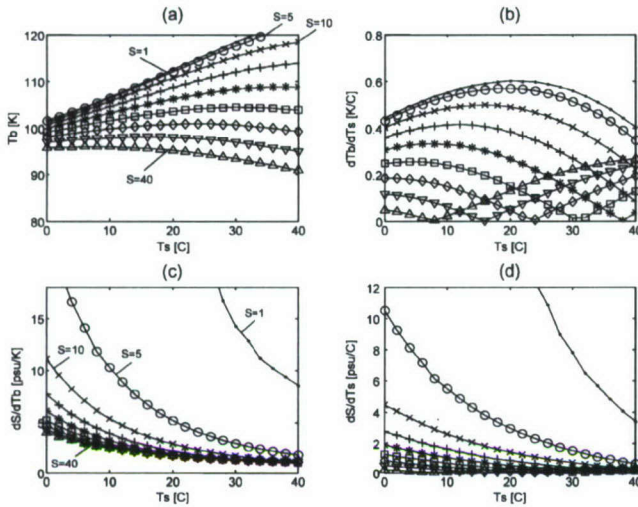As previously mentioned for salinity, the relationships involving Tb and D were computed for V-Pol signals at an

Fig. 2. SSS algorithm sensitivities, given S values in the range [1,5:5:40 psu] for an incidence angle of $22°$, vertical polarization, and a frequency of 1.4 GHz. (a) S as a function of Ts and Tb. Sensitivity along the isohalines of (b) Tb to Ts versus Ts, (c) S to Tb versus Ts, and (d) S to Ts versus Ts.

incidence angle of $22°$ relative to nadir. The plots quantitatively differ at other incidence angles but show the same qualitative features. For economy, and considering that STARRS has a single V-Pol mode, we exclusively use V-Pol in all subsequent calculations in this paper, but analogous results can be obtained for other polarization modes.

The application of the SSS retrieval algorithm, which utilizes the KS77 relation [replotted in Fig. 2(a)], proceeds by assuming a starting (first guess) salinity and using the observed Ts value to compute a corresponding Tb for a given instrument beam incidence angle and polarization. Typically, Ts will either be measured in situ or remotely from satellite or airborne IR or microwave radiometers, with appropriate corrections for atmospheric effects, to ensure that it is accurate at the sea surface. The computed Tb value then represents the brightness temperature that would be observed by the instrument, at the sea surface, given its associated incidence angle and polarization state. This value is propagated through the atmosphere to the remote sensing platform, allowing for environmental influences such as reflected extraterrestrial and atmospheric (O_2) radiation, enhanced emission and modified reflection due to a roughened sea surface, and atmospheric absorption. The resulting brightness temperature is compared with the observed antenna temperature. If these do not match within a specified tolerance, the starting salinity is adjusted (based on a gradient descent algorithm), and the process iterates until convergence is attained.

The development of an alternative algorithm for density retrieval that involves a direct empirical relationship between Ts, D, and Tb for a given S and θ could also be considered. Such an algorithm could be expressed in the form of the D curves in Fig. 1(a). However, we are aware of no practical technique to directly observe density in the ocean; other indirect techniques such as measurement of refractive index are less accurate and less practical than the conventional methods of determining it from field observations of Ts and S using a well-calibrated

conductivity temperature depth (CTD) profiler. Direct determinations of seawater density in a laboratory, e.g., through diluting or evaporating seawater and measuring corresponding masses and volumes, are also difficult to accurately perform in comparison with laboratory salinometer measurement of seawater samples. Given that the practical salinity scale [21] defines S in terms of the conductivity of a standard KCl solution and that the microwave radiometers respond to brightness temperatures that are largely determined by the conductivity of seawater, the approach based on the sequential application of the empirical KS77 and SES appears to be the most practical.

B. Algorithm Uncertainties

For the chained KS77 and SES density retrieval algorithm, uncertainties will arise from observational biases and random errors in the observed Ts and Tb, which are input to the algorithm, and from the combined effect of uncertainties in the empirical relationships for determining both S and D. The latter uncertainties could arise from inaccuracies in the laboratory data as well as from errors in the regression model fits used to determine these empirical relationships.

1) Accuracy: The claimed accuracy of KS77 based on various concentrations of standard mean ocean water is 0.3 K or better in brightness temperature. While the KS77 relation was determined from conductivity measurements using a microwave resonant cavity containing samples of seawater from Chesapeake Bay and the Pacific Ocean as well as NaCl solutions, the algorithm has not yet been related to the new KCl conductivity standard upon which the Practical Salinity Scale 1978 [21] is based. An alternative seawater emissivity model by Ellison et al. [8] is also available. This employed samples of natural and synthetic seawater and also NaCl solutions. The latter solutions were found to have a significantly different permittivity than the seawater samples. This suggests that there might be difficulties in transferring the permittivity algorithms to the new KCl standard. The Ellison et al. emissivity model reportedly performs better than KS77 at high microwave frequencies but is less accurate than KS77 at lower microwave frequencies (including the L-band). Recent laboratory and field experiments by Blanch and Aguasca [22] and Wilson et al. [23] support an accuracy of ±0.1 K for KS77, which is presently considered the de facto "standard" for work at L-, S-, and C-band. These are the most useful bands for surface salinity, temperature, and roughness retrievals and are thus most relevant to passive remote sensing of SSS.

The standard error associated with fitting data to the regression model to form the SES is given as 3.6×10^{-3} kg·m^{-3} in [24]. The accuracy of the fitted data itself was not reported, but since the SES is the virtual standard for computing seawater density from T and S, we assume that this error can be neglected. We focus instead on how instrument bias and, particularly, random errors for Tb and Ts propagate through the resulting (chained) nonlinear retrieval algorithm. Given the expected observational errors in remotely sensing SST and SSS, the resulting S and D errors turn out to be significantly larger than the expected errors due to laboratory data inaccuracies or regression model misfit in the empirical formulation of KS77
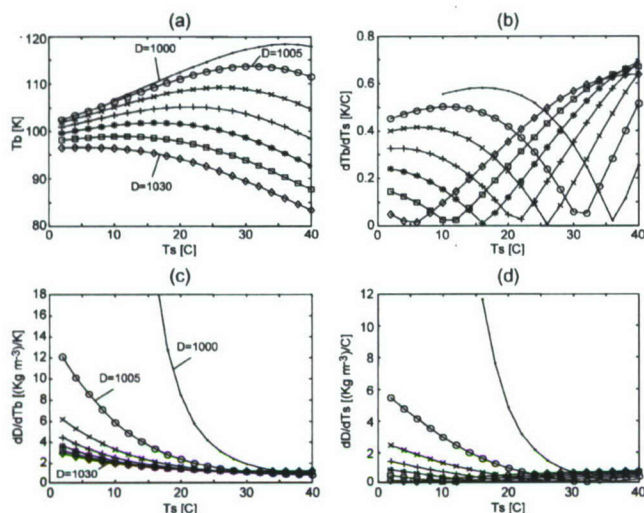
Fig. 3. SSD algorithm sensitivities, given D values in the range $[1000:5:1030 \text{ kg} \cdot \text{m}^{-3}]$ for an incidence angle of $22°$, vertical polarization, and a frequency of 1.4 GHz. (a) D as a function of Ts and Tb. Sensitivity along the isopycnals of (b) Tb to Ts versus Ts, (c) D to Tb versus Ts, and (d) S to Ts versus Ts.
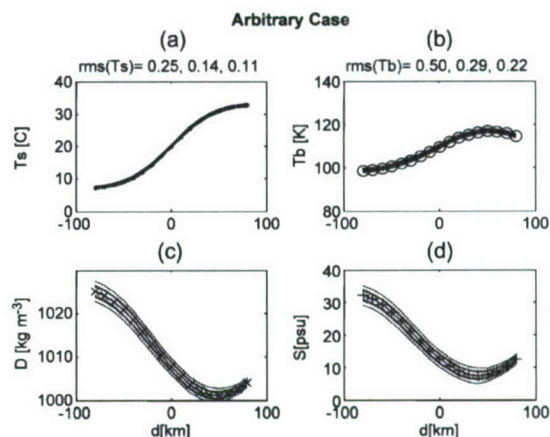

Fig. 4. Idealized horizontal transects of (a) SST and (b) Tb with given rms error levels and the corresponding (c) SSD and (d) SSS with computed 95% error bounds. The Ts and Tb profiles were arbitrarily chosen, so that horizontal variations in Ts and S mutually reinforce or compensate that of D at different locations. An incidence angle of $22°$ was assumed.

and the SES. Thus, KS77 and SES model errors are negligible compared with the effects of present-day measurement error levels in Tb and Ts when deriving errors in S and D.

2) Sensitivity: Since the predicted brightness temperature Tb is (at first order) proportional to the SST Ts with a "constant" of proportionality (the emissivity), being itself a function of temperature and salinity, Tb is sensitively and nonlinearly related to Ts. This sensitivity is demonstrated [Fig. 2(b)] by the absolute value of the derivative of Tb with respect to Ts versus Ts for the given values of S, as determined by KS77 [Fig. 2(a)]. While Figs. 1(a) and 2(a) present Tb as a function of Ts, Fig. 2(b) presents the absolute value of the slope (first derivative) of Tb with respect to Ts versus Ts. Points of zero slope, i.e., minimum sensitivity, correspond to the turning points traced by the dotted lines in Fig. 1(a). These points where slope changes sign from positive to negative at higher Ts values appear in Fig. 2(b) as "reflections" of the absolute value of the slope along the Ts-axis. Points of maximum slope, i.e., maximum sensitivity, which appear in Fig. 1(a) where the parametric curves are steepest, correspond to the turning points (maxima) of the curves in Fig. 2(b). Fig. 2(b) thus shows that the minimization and maximization of the Tb versus Ts slope occur within certain portions of the Ts range and at progressively higher temperatures for successively lower salinities. It is at the maxima that Ts errors will most adversely impact the determination of Tb.

Corresponding sensitivities of S to Tb [Fig. 2(c)] and Ts [Fig. 2(d)] as a function of Ts exhibit a monotonically changing negative slope as a function of increasing Ts, clearly showing that the largest SSS retrieval errors due to instrumental errors in Tb and Ts will occur at the colder temperatures and the lower salinities. The sensitivity of S to Ts is almost zero at the highest salinities [Fig. 2(d)], but its sensitivity to Tb remains significant, even at the highest Ts and S values (where it asymptotes to about 1.6 psu/K). From the perspective of salinity retrieval, we note that high sensitivity of S to Ts is

a disadvantage to the extent that errors in Ts will adversely impact the retrieval, whereas low or even zero sensitivity is advantageous. Similarly, high sensitivity of S to Tb is a disadvantage, because it amplifies the effects of Tb errors, whereas low sensitivity is advantageous. In this case, zero sensitivity would be undesirable, because a complete lack of dependence of S on Tb would make the retrieval of S from Tb impossible!

For the derivation of density from the combined empirical relations for SSS and D [Fig. 3(a)], the patterns of sensitivity to the observables Tb and Ts are similar to those of S, as previously discussed. The sensitivity of Tb to Ts, given D [Fig. 3(b)], although similar to that given S [Fig. 2(b)], has both its turning and reflection points shifted toward colder Ts values and a maximum occurring for the least dense water $(1000 \text{ kg} \cdot \text{m}^{-3})$ at the high-temperature end. This is due to the slopes of D tending to be more negative than those of S at higher Ts, as revealed in Fig. 1(a) (where the turning points for D traced by the dotted lines fall to the left of those of S). The sensitivities of D to Tb and Ts [Fig. 3(c) and (d)], as a function of Ts, all show similar patterns to those of S.

To illustrate how random observational errors in Ts and Tb impact the retrieval of S and D under a representative range of T and Tb values, we define an idealized spatial transect of Ts and Tb, with an arbitrary distance scale and origin $(d = 0)$ at the center of the transect, that could represent a strong continental shelf scale frontal contrast (Fig. 4). This might be encountered in wintertime shelf circulation when a warm western boundary current, such as the Gulf Stream, impinges on the outer continental shelf. In this case, Ts [Fig. 4(a)] is chosen to increase monotonically seaward, whereas Tb similarly, but arbitrarily, increases in the same direction and finally decreases at the seaward end. These "observed" Ts and Tb values were used to perform a simulated salinity and density retrieval in the presence of representative random (root mean square, rms) errors in the raw Ts and Tb observations of 0.25 °C and 0.5 K, respectively. Although arbitrarily chosen, these values approximate those estimated for 30-day averaged SMOS data [see Section II-C and Table I(b)]. The resulting mean D distribution

TABLE I
INPUT SAMPLING PARAMETERS, AND SST, WS, AND Tb ERRORS FOR SSD RETRIEVAL

(a)

Instrument	IR SST Stdev K	L-band Tb Stdev K	L-band Integration Time s	Averaging Period	SST (& WS) N_{df}	Tb N_{df}
STARRS	0.70	0.21	24.0	1 min	1	2.5
SMOS	0.70	4.00	1.2	30 day	10	50
Aquarius	0.70	0.06	12.0	28 day	4	4

(b)

	Nominal Pixel Size km	Ts noise Stdev K	Tb Noise Stdev K	Wind Spd Stdev m/s	Wind Noise Stdev K	Total Tb Noise Stdev K
STARRS	5	0.70	0.13	1.5	0.21	0.25
SMOS	50	0.22	0.57	1.5	0.03	0.57
Aquarius	80	0.35	0.03	1.5	0.06	0.07

(c)

	Incidence Angle deg	Ts bias Rms K	Tb Bias Rms K	Wind Spd Bias Rms m/s	Wind Tb Bias K	Total Tb Bias Rms K
STARRS	22	0.10	0.71	0.5	0.07	0.71
SMOS	40	0.20	0.40	0.5	0.03	0.40
Aquarius	34	0.20	0.10	0.5	0.04	0.11

[Fig. 4(c)] shows a substantial decrease offshore that is driven by the Ts increase (with warmer water of the same salinity being less dense), but it starts to increase at the outer end while Ts merely levels off. Reference to the retrieved salinity [Fig. 4(d)] shows that the density trend reversal was associated with an increase in S at the outer shelf end of the transect (near $d = 40$ km). Confidence bands (at the 95% level) given for rms error levels corresponding to raw and (three- and five-point box car) filtered data are shown for the input T and Tb values and the output D and S values. While these bands are proportionally small and uniform across shelf for Ts and Tb, they are proportionately wider but decrease in width across shelf for D and S. The reduction in rms error in the outer shelf is due to the decreased sensitivity of D and S to Ts and Tb errors experienced in warmer waters [Figs. 2(c) and (d) and 3(c) and (d)].

Both the S and D retrieval errors were computed using two different methods. The first assumed that both the input and output errors were normally distributed and defined the 95% confidence limits as being twice the standard deviation of the series. The retrievals were then performed on both the mean values and the upper and lower bounds of Ts and Tb. In this way, the error limits were propagated through the retrieval algorithm by applying the same equations to the limits that were used to transform the mean values. The second method employed Monte Carlo simulation to deduce the rms errors. This was done by generating a large number of realizations of the Ts and Tb space series using error time series produced by a random normal number generator. The retrievals were then performed on each realization of the ensemble, and the

results were statistically analyzed to determine the mean and rms errors of D and S. Since both methods produced virtually identical results, the first method was subsequently employed, because it was computationally faster.

C. Density Retrieval Errors

Representative SSD retrieval errors, both systematic and random, are now estimated for selected sampling configurations and parameters of SMOS and Aquarius. These are needed to evaluate potential applications of the satellite sensors and to determine the utility of STARRS for testing satellite retrieval algorithms. The diverse technologies, sampling capabilities, and operational configurations of these instruments do not allow a comprehensive analysis. This would require the application of various simulation methods, e.g., [25]–[29], and is outside our scope. Instead, we select representative sampling parameters (Table I) for typical operating conditions of each system. The intent is not to compare and contrast sensor performance, which varies over a wide parameter range and can be optimized for specific purposes, but to indicate expected error levels when retrieving SSD under conditions that are typical for each instrument. Although several environmental corrections are needed to minimize noise and bias in SSS and SSD retrievals (see Section II-A), we focus on SST and wind-induced sea surface roughness (SSR), which exert the most influence on the retrieval errors. STARRS Ts and Tb errors were estimated from laboratory and field studies ([30], whereas representative Ts, Tb, and associated wind-induced noise and bias values for SMOS and Aquarius were obtained from the literature (e.g., [26], [27], [31], and [32]). We discuss random errors first and then show how they combine with systematic errors to determine the total SSD error due to Ts and Tb.

Estimated single-sample errors, which are expressed as standard deviations Sdv for Ts and Tb Table I(a) (columns 1 and 2) were determined from laboratory and field measurements. The SST values are the Sdv's of the residual errors of observations from the onboard IR radiometer (for STARRS) and from the National Oceanic and Atmospheric Administration (NOAA) Advanced Very High Resolution Radiometer data (for the satellites), compared with *in situ* observations, after atmospheric water vapor correction. Tb values correspond to the effective noise equivalent delta temperature (or radiometric sensitivity) of each L-band radiometer for the specified integration time (column 4). For the random error analysis [Table I(b)], the single-sample data acquired at the nominal pixel sizes (column 2, given for illustration but not used in the calculations) are assumed to be temporally averaged over a given period [Table I(a) (column 5)]. For STARRS, this implies spatial averaging over a 5-km distance along track in a single overpass (the actual sampling times and pixel sizes are ~2 s and 1 km, respectively; see Appendix A-1). We could average successive daily overflights of STARRS over, for example, a ten-day period, but salinity distributions in coastal areas, where it is typically flown, vary significantly on daily time scales, so aliasing errors would be large. For satellite observations over the deep ocean, which vary on much longer time scales, averaging of data from particular pixels during successive repeat orbits is assumed. For

SMOS, which is an imaging interferometer, successive multi-angle views acquired along the "dwell line" provide additional samples for temporal averaging [27]. Hence, the corresponding number of degrees of freedom N_{df} (or the effective number of independent samples) for Tb [Table I(a) (column 6)] is the least for STARRS and the most for SMOS. SST and wind observations are assumed to be acquired near each L-band pixel only once per orbit, so their N_{df} [Table I(a) (column 4)] is generally smaller than that for Tb. For SMOS and Aquarius, temporal averaging is more efficient than spatial averaging due to spatially correlated environmental correction and instrument errors [27]. While the actual pixel sizes and incidence angles for each instrument vary over a significant range (e.g., 32–100 km and 0° to 65° for SMOS [5]), only nominal midrange values are used here. Although the data from both the SMOS and Aquarius missions will be spatially averaged at ∼300-km resolution to produce monthly global salinity products, with a target precision in the range of 0.1–0.2 psu, we assume, for simplicity and to preserve resolution, that no spatial averaging is performed (with the exception of STARRS, as previously noted). To account for noise reduction by temporal averaging, we assume independent Gaussian random samples and reduce the sampling Sdv [Table I(a)] by a multiplicative factor of $1/\sqrt{N_{df}}$ to determine effective noise levels Table I(b) (columns 3 and 4) for IR Ts and L-band Tb, respectively. For the L-band, there is an added contribution from (primarily wind-induced) SSR. The wind speed random error of 1.5 m · s^{-1} (column 5) is representative of available buoy data and satellite-observed or model-analyzed ocean wind products. Using this value with the incidence angles [Table I(c) (column 1)] in the Camps *et al.* [33] empirical formula (for V-Pol) yields the wind impact on rms Tb noise levels [Table I(b) (column 6)]. These are added to the instrument Tb noise (using root sum of squares addition) to yield the total Tb random noise level [Table I(b) (column 7)]. The Ts (column 3) and Tb (column 7) noise levels are separately input into the algorithm to determine their impact on random errors in SSS and SSD retrievals through the combined effect of KS77 and the SES. For each $T-S$ pair in a preassigned matrix spanning their observational range, the sensitivity of SSS and SSD (Figs. 2 and 3) to errors in Ts and Tb is multiplied by the corresponding Ts and Tb noise levels Table I(b) (columns 3 and 7) to produce a map of SSD random errors in the $T-S$ space [Fig. 5(a), (c), and (e)].

In contrast to random errors, which are reduced by averaging, bias estimates are not reduced. Being thus simpler to statistically treat, they are harder to estimate in practice, because of the difficulty of establishing absolute reference values in the field. The biases for Ts [Table I(c) (column 3)] were estimated from published comparisons of water-vapor-corrected SST product values with *in situ* buoy data, e.g., [34] and [35], whereas the instrument Tb biases (column 4) were determined from actual laboratory data (STARRS [30]) and from simulation or prototype tests (SMOS and Aquarius [31], [32]) giving expected calibration drift over one month. The wind bias (column 5) was estimated from comparisons of various satellite wind sensor products and buoy winds, e.g., [36]. The instrument and wind-induced Tb rms biases and noise levels were finally added together (in the rms sense), to determine the total Tb error

(column 7) for input into the retrieval algorithm, along with the corresponding Ts errors (column 3).

The resulting SSD error maps (Fig. 5) exhibit a broad elliptical minimum stretching between the high T and S-axis values, with a focus mostly near high T. The errors generally increase as SST and SSS values decrease and ultimately reach levels that are unacceptably large for any conceivable application (in excess of 3 kg · m^{-3}). The total (random plus systematic) error shown in the right-hand panels is minimized for warm SSTs and midrange SSS, and is low (∼0.25) for Aquarius, due mainly to its exceptional Tb stability and noise performance. It is marginal (exceeding 1 kg · m^{-3}) in the midranges for STARRS and SMOS. The random errors isolated in the left-hand panels follow a similar distribution but are significantly lower than the total errors for SMOS, and particularly STARRS, which has a relatively good noise performance but poorer calibration stability. The SSD error variation (black contours) is approximately orthogonal to that of density (white contours), so the two quantities are virtually uncorrelated. In any case, the density errors are on the order of 1 : 1000 kg · m^{-3} or 0.1%. However, the errors expressed in units of σ_t as a percentage of the range of density variation of the world's ocean ∼35 σ_t(1035 kg · m^{-3} − 1000) are more pessimistic, being ∼1% at best and rapidly climbing above 10% at SSS levels of below about 15 psu, which is typical of estuarine plumes. The SSD error levels for all three systems ∼0.5 kg · m^{-3} (or 0.5 σ_t) for the T and S values typical of temperate and tropical climates appear adequate for determining density gradients, at least in more saline areas, and where density fields vary significantly on scales exceeding 100 km.

III. DENSITY VARIATION

Based on the preceding idealized SSD error analysis and the more realistic cases of STARRS, SMOS, and Aquarius, we now consider how SST and SSS variations and errors may compensate or reinforce one another to influence retrieved SSD and its errors. We then evaluate the potential to determine SSD gradients with sufficient precision to determine near-surface geostrophic shear from SST and SSS mapped by the IR and microwave satellites.

A. Compensation and Reinforcement

The somewhat arbitrary distribution of Ts and Tb [Fig. 4(a) and (b)] resulted in a retrieved S [Fig. 4(d)] that was largely anticorrelated with Ts (except in the outer shelf where Ts leveled off). This represents an interesting case of mutual reinforcement in which the T and S variations both contribute to a decrease in D (as T increases and S decreases). In this situation, D variations will always be large when (both) Ts and S variations are large. Consequently, frontal systems may be best detected by identifying regions of strong density variation. The reinforcement case may occur in summer when warm water near shore contributes to low near-shore densities that are reinforced by runoff from large rivers with persistent annual flow (or little seasonal variation). This could be illustrated by the case shown in Fig. 4 if the coast is considered to lie on
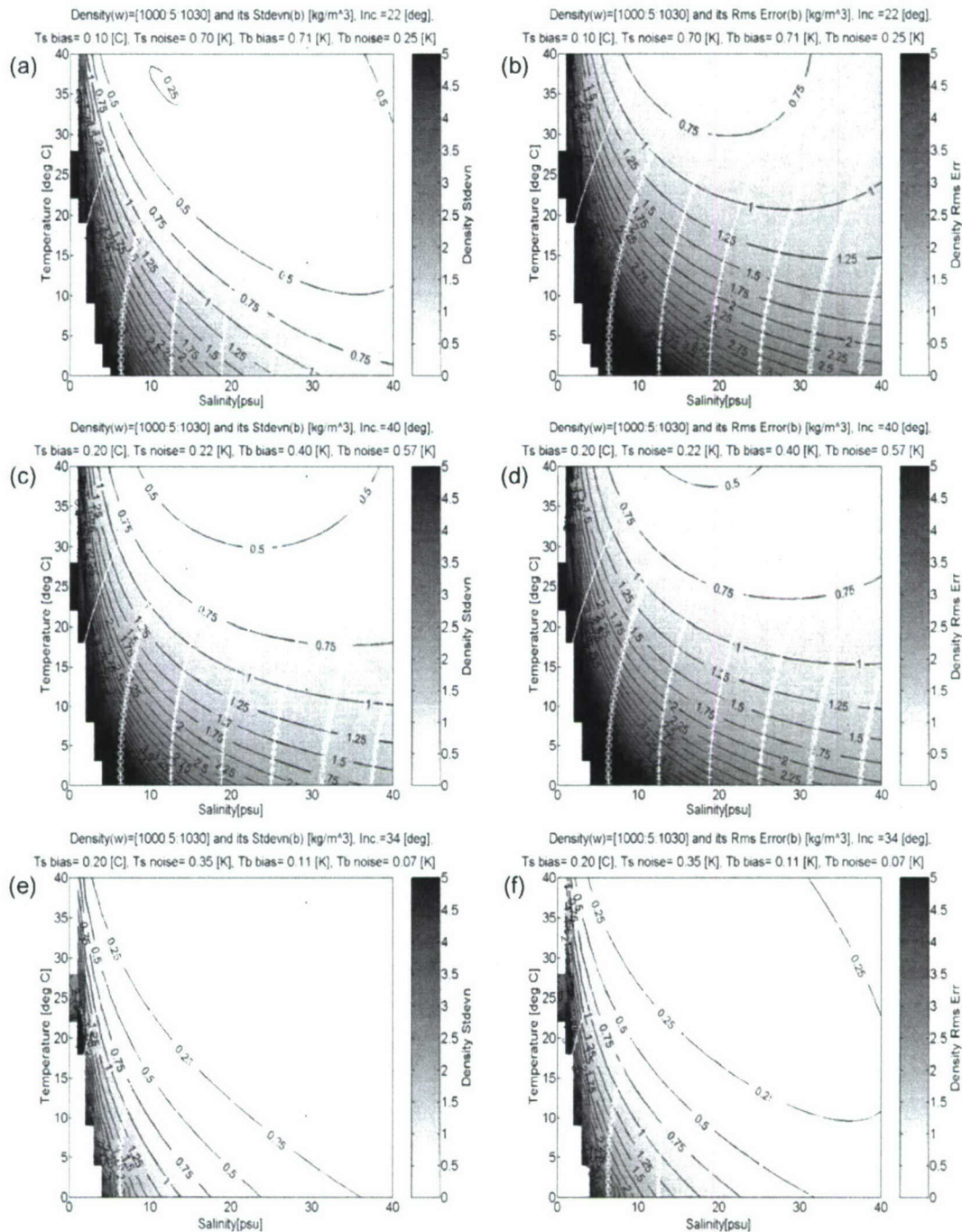
Fig. 5.   (a), (c) and (e) Random and (b), (d) and (f) total (i.e., random plus systematic) SSD error (grayscale with black contour lines) as a function of SST and SSS for representative configurations of (a) and (b) STARRS, (c) and (d) SMOS, and (e) and (f) Aquarius. The white contour lines with markers represent SSD ranging from 1000 to 1030 (left to right) in 5-kg · m^{-3} steps [as in Fig. 1(b)].

the right-hand side (RHS), rather than on the left, as in the preceding discussion.

The opposite case of compensation is also surprisingly common in oceanographic settings. For example, in temperate regions during winter, cooler water near the coast may coincide with freshwater associated with winter runoff. Cases of compensation also occur in frontal systems that are equilibrated by strong vertical mixing processes operating at the frontal interface (e.g., salt fingering). In the Middle Atlantic Bight of the U.S. east coast, cool freshwater likely derived from the ice melt

in the Labrador Sea (forming the so-called "Cold Pool"; see [12] for sample sections) may lie shoreward of and/or underneath the warm saline slope water derived in part from the Gulf Stream. In such cases (e.g., Fig. 6), Ts and S both increase seaward, so their variations are correlated and they have a mutually compensating effect on the resulting D variation. Consequently, the density contrast may be weak or even absent, whereas Ts and S variations are strong, and fronts may not be detected in density retrievals, even though they are strongly evident in Ts and S retrievals. In Fig. 6, we dispensed with the error bounds,
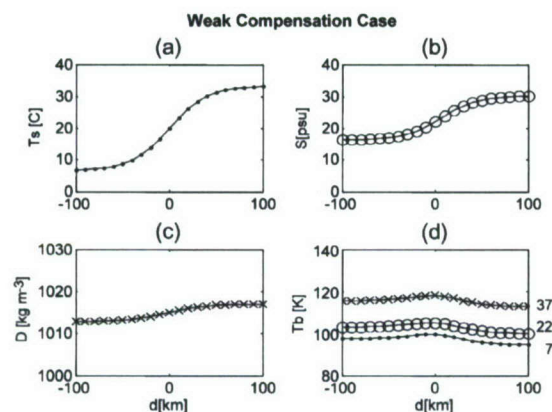
Fig. 6. Idealized horizontal transects of (a) SST and (b) SSS, and the corresponding (c) SSD and (d) Tb. The Ts and S profiles were chosen, so that their horizontal variations mutually and weakly compensate in their effect on D. The corresponding Tb for incidence angles of $7°$, $22°$, and $37°$ are also shown in (d). Error bounds for D in this case are shown in Fig. 9(c).

in favor of showing how Tb varies with incidence angle. However, the uncertainty in the D variation is illustrated for the arbitrary and weak compensation cases in Figs. 9 and 10. For the latter case, the across-shelf density gradient is not resolved.

B. Density Compensation Index

Given the importance of density reinforcement and compensation processes in physical oceanography and the emerging possibility of determining density from salinity mapping satellites, it is instructive to employ an index that can be mapped in a survey area to help determine the potential dynamical significance of ocean fronts associated with strong temperature and salinity contrasts. Apart from knowing whether T and S are mutually reinforcing or compensating with respect to density, it is also of interest to determine which of T and S play the dominant role in determining D. This can be useful in developing numerical hydrodynamic models to simulate likely contributions to model density fields from such diverse factors as freshwater runoff, solar heating, and ice melt. To serve both these purposes, we employ a vector index (the "Turner vector," presented in Appendix B), which is a simple extension of the Turner angle defined by Ruddick [18] for studying double diffusive activity. This angle is defined in terms of the density ratio used by oceanographers to study ocean stratification and fine structure. Johnson [19] adapted the Turner angle to study density compensation in horizontal T and S gradients. He projected the local horizontal salinity gradient onto the direction of the local horizontal surface temperature gradient (which, in the deep ocean, is mostly equatorward). This provided the reference direction for computing the "horizontal" Turner angle, enabling large areas of the world's ocean with density compensating salinity gradients to be identified. In our coastal work, the across-shelf direction is a convenient reference direction, which closely approximates the directions of the prevailing T, S, and, hence, D gradients through the high-aspect-ratio Plata plume.

The Turner vector can be used to indicate either density reinforcement or compensation by T and S while taking into

account the relative dominance and absolute significance of T and S variations in their effect on D. To illustrate its application to various idealized oceanographic settings, we consider a variety of cases including strong reinforcement with salinity dominance [Fig. 7(a)]; weak compensation with S dominance [Fig. 7(b)]; the arbitrary variation switching from reinforcement to compensation with S dominating, except during the transition when T dominates for a short distance [Fig. 7(c)]; and finally the case of a linear variation in density across shelf, which results in reinforcement mostly dominated by S variations [Fig. 7(d)]. The cases of weak compensation and arbitrary variation are those presented in Figs. 4 and 6, respectively. The strong reinforcement case was created from arbitrary but opposing T and S gradients. The linear case was created from an arbitrary nonlinear across-shelf T and a linear D pattern with the corresponding Tb (and S) computed using the SES and KS77 algorithms in the forward (instead of the usual inverse) computation modes. This somewhat artificial reinforcement case was created to illustrate how a linear D variation in space could (and in fact must) result from nonlinear T and S variations due to the inherent nonlinearities of the algorithm. The perfect compensation case $(dD/dx) = 0$ is a special case of a linear D variation, with zero across-shelf gradient. These two cases also illustrate how quite different patterns of T and S reinforcement or compensation can produce density distributions that are similar in character, i.e., D profiles are not uniquely determined by T and S.

The Turner vector values for the cases shown in Fig. 7 may be displayed more compactly in a polar diagram (Fig. 8), which is a variant of the approach used by Ruddick [18], which is explained in Appendix B. This method of presentation displays variations of the Turner angle and magnitude for different transects in a compact diagram but does not explicitly reveal the pattern of across-shelf variation evident in Fig. 7.

IV. HORIZONTAL GRADIENT AND GEOSTROPHY

In the previous sections, we considered how SSS and SSD may be derived using existing salinity retrieval algorithms, combined with the SES. We also examined associated retrieval uncertainties and considered the nonlinear influence of various spatial distributions of Ts and Tb on the spatial distribution of D. The resulting density gradients may be weak or strong, depending on whether Ts and S are either weak or mutually compensating, or else mutually reinforcing. These have significant impact on the dynamics of ocean circulation. One significant impact, which is widely recognized by physical oceanographers, is its effect on horizontal pressure gradients and, hence, on buoyancy-driven currents. Geostrophy theory depends on a simplified momentum balance, in which the Coriolis and horizontal pressure gradient terms cancel, whereas the other terms are negligible. Widely used in classical meteorology and oceanography to determine mean ocean currents and winds, it has recently come to the forefront again, with the advent of high-performance spaceborne altimeters (e.g., TOPEX and Jason). These can resolve SSH with an accuracy of about 5 cm and a precision of 2 cm or better. They can be used to determine sea surface slope variations with respect
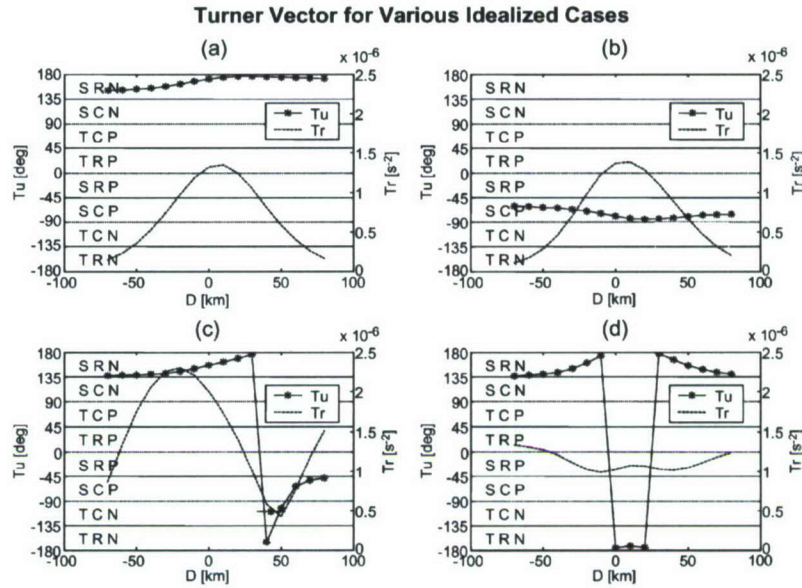
Turner Vector for Various Idealized Cases

Fig. 7. Turner vector plots shown in Cartesian component form as a function of across-shelf location. The cases shown are idealized transects exhibiting (a) reinforcement, (b) weak (under-) compensation, (c) arbitrary density variation, and (d) linear density variation. Cases (b) and (c) correspond to the profiles shown in Figs. 6 and 4, respectively.
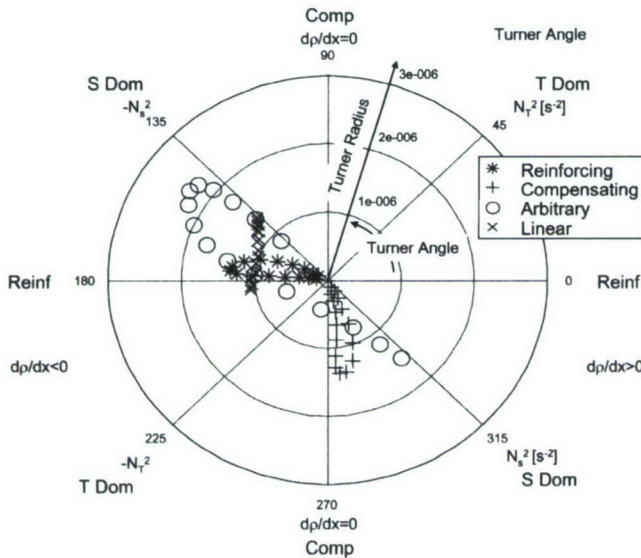

Fig. 8. Turner vector plots shown in polar form, corresponding to the idealized transects shown in Fig. 7, i.e., ($*$) reinforcement, (+) weak (under-) compensation, (o) arbitrary density variation, and ($\times$) linear density variation.

to the mean ocean surface topography, from which surface geostrophic currents can be determined. Along with accurate geoid observations from gravity missions such as Champ and GRACE, this makes possible the determination of absolute (i.e., Earth relative) mean and fluctuating ocean currents due to horizontal pressure gradients expressed at the surface.

The possibility of mapping SSD from space raises the prospect of computing the vertical shear of the geostrophic currents at the surface to give an indication of subsurface current profiles driven by horizontal pressure gradients arising from surface and internal density differences. If we assume that horizontal density gradients $dD(x)/dx$ are independent of depth (at least, within a depth range of interest), while the

density linearly increases with depth, we obtain a formula for the total geostrophic current V_g at depth z (see Appendix C for details of its derivation and notation), i.e.,

$$V_g(z) = \frac{g}{f} \cdot \frac{d\xi}{dx} - \frac{gz}{fD(x)} \frac{dD(x)}{dx}. \tag{1}$$

Here, g and f are the acceleration due to gravity and the Coriolis constant, respectively, and ξ is the sea surface elevation relative to the mean sea level. The two right-side terms, which we denote as V_e and V_i, result from pressure gradients driven by the external sea surface slope and internal density differences, respectively. V_e can be obtained by deriving SSH gradients from satellite altimeters, whereas V_i can be obtained, as demonstrated in this paper, by deriving horizontal density gradients from L-band radiometers using a variant of the "thermal wind" equation. At the surface, $V_i = 0$, so the surface geostrophic velocity $V_g(0) = V_e$, whereas, at depth z, $V_i(z)$ represents the deviation of the geostrophic velocity from that at the surface. In meteorology and oceanography, the term "velocity shear" is commonly used to describe this deviation, but we prefer to apply this term to the vertical velocity gradient dV_g/dz.

By assuming that $dD(x)/dx$ is constant throughout a near-surface layer of specified depth, we can project the vertical shear at the surface downward to determine the geostrophic current throughout the layer. This assumption may be expected to hold in a variety of situations such as in continental shelf fronts during winter when the large-scale stratification is not perturbed by the seasonal pycnocline and along the margins of the deep ocean gyres away from intense western boundary currents, which may be bounded by nonlinear meanders and mesoscale eddies. We will show later that this assumption is justified in the large-scale wintertime Plata river plume. The assumption, together with the results of a dimensional analysis demonstrating that the across-plume momentum balance is
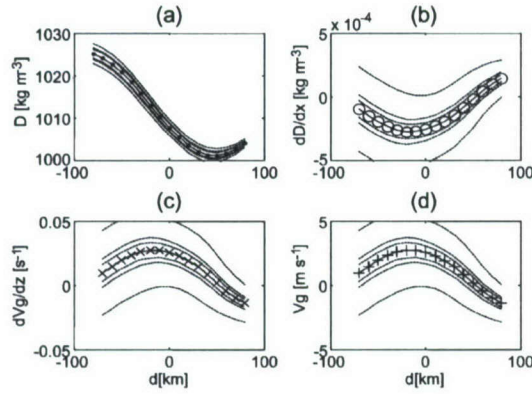
Fig. 9. Derivation of geostrophic current at the base of the surface layer with 95% error bounds for simulated raw and filtered data for the case of arbitrary horizontal SST and SSS variation. The raw rms errors for Ts and Tb were 0.25 °C and 0.5 K, respectively. The box car filters were one, three, and five points long. The transects shown are for surface (a) density, (b) horizontal density gradient, (c) geostrophic shear, and (d) geostrophic velocity at depth (z_0), relative to the surface. This case corresponds to the arbitrary SSS and SST transects shown in Fig. 4.
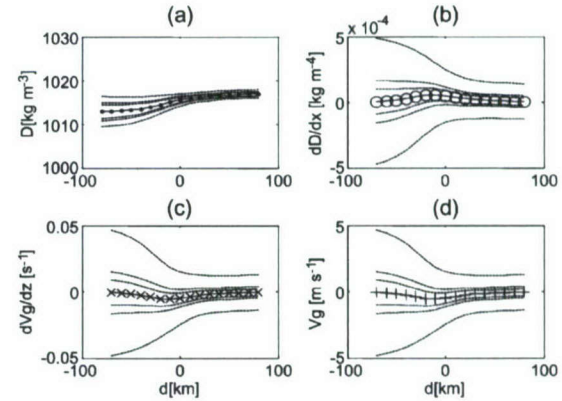

Fig. 10. Derivation of geostrophic current, as in Fig. 9, but for weakly compensating SST and SSS variation (the other parameters are as in Fig. 9). The transects shown are for surface (a) density, (b) horizontal density gradient, and (c) geostrophic shear, and (d) geostrophic velocity at depth (z_0), relative to the surface. This corresponds to the weakly compensated transect of Fig. 6.

geostrophic, can be used to estimate the subsurface geostrophic current on the continental shelf.

If, for the moment, we assume that the surface geostrophic velocity $V_e = 0$, then the geostrophic current at the base of a near-surface layer of thickness H is just the internal velocity given by (1), i.e.,

$$V_g(H) = V_i(H) = -\frac{gH}{fD(x)} \cdot \frac{dD(x)}{dx}. \qquad (2)$$

This calculation may be illustrated by using an idealized case, which also allows the resulting error bounds on the geostrophic velocity to be determined. For the arbitrary case presented earlier [Fig. 9(a)], the horizontal density gradient [Fig. 9(b)] is negative near the center of the transect, with smaller errors in both D and dD/dx due to the warmer temperatures at the outer shelf end [Fig. 4(a)]. The random errors are amplified by the differencing operation; hence, spatial filtering is necessary. Since bias errors due to instrument drift will be largely, if not completely, eliminated by the differencing operation, we have chosen not to simulate them here. The resulting geostrophic shear (or vertical velocity gradient) [Fig. 9(c)] and geostrophic current (relative to the surface) at the base of a 200-m-deep layer [Fig. 9(d)] show that, for the specified Ts and Tb error levels, and modest (three- or five-point box car) filtering, the errors can be reduced to the point where the across-shelf geostrophic current variations are well resolved. Recall that, in the arbitrary case, the density variation is dominated by salinity but reinforced by the temperature variation. This may be contrasted with the weak compensation case [Fig. 10(a)], for which the errors in the computation of dD/dx, dV_g/dz, and $V_g(z_0)$ (Fig. 10(b)–(d), respectively) almost swamp the signal, in spite of the spatial filtering. Thus, the geostrophic current calculation will succeed only in certain regions and seasons when the SSD signal-to-noise ratio is sufficiently high to resolve the across-shelf variability.
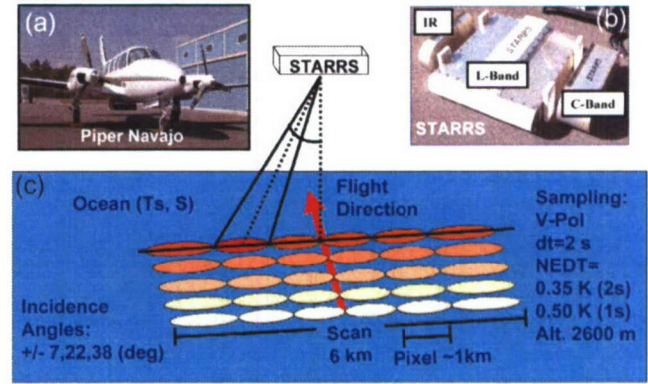

Fig. 11. (a) STARRS aircraft with the instrument mounted underneath, (b) instrument system comprising L-, C-, and IR-band radiometers, and (c) L-band instrument six-beam sampling pattern. The average pixel size is 1 km at a nominal 2600-m flight altitude.

V. APPLICATIONS

STARRS [Fig. 11] is an airborne radiometer system designed to map SSS, SST, and SSR with a spatial resolution of about 1 km over rectangular domains with linear dimensions of about 60 km in a 4-h flight. (See Appendix A-1 for a description of the instrument and its calibration, and [30] for details on instrument performance.) Surveys of the Mississippi River plume were conducted using STARRS in the early boreal summer in May and in the early winter in November 2004 [37]. Surveys of the Plata River plume were conducted in the austral winter in August and September 2003 and in the summer between January 30 and February 10, 2004. (See [38], [39], and Appendix A-2 for details on the survey operations and data processing.) Only SSS and SST were successfully surveyed, as the C-band instrument designed to measure SSR suffered excessive calibration noise (since remedied), so the roughness effects could not be directly observed. Instead, wind speed observations from meteorological buoys and ships were used to perform roughness corrections based on the Camps *et al.* [33] empirical formula. The survey data were used here to study the seasonal variation in density distribution, as illustrated by the
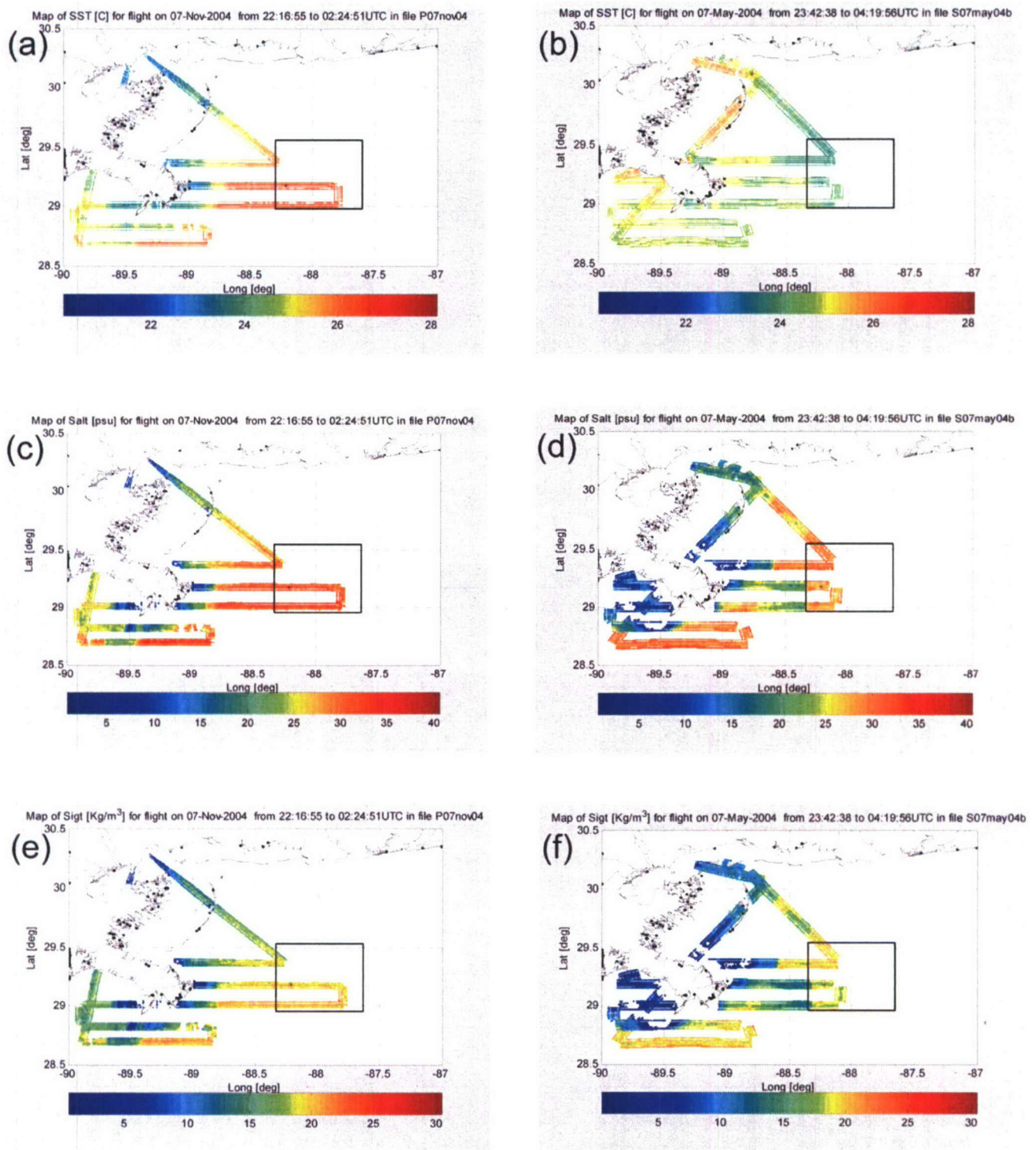
Fig. 12. Seasonal density contrasts for the Mississippi River plume from STARRS SST, SSS, and SSD maps for (a), (c), and (e) winter and (b), (d), and (f) summer with Ts and S effects compensating and reinforcing, respectively. In both cases, S dominates T in its effects on D. The box encompasses the area occupied by the SEED mooring array. Asterisks mark the respective northwest and southeast locations of NOAA data buoys 42 007 and 42 040. The IR radiometer nadir view of SST (a) is repeated across track, and all swath widths are exaggerated by a factor of 2 for clarity.

results obtained for the Mississippi plume, and the across-shelf variation of near-surface geostrophic velocity, as illustrated using the Plata plume results.

A. Seasonal Density Contrasts

Representative STARRS SST survey results for the Mississippi River from the winter flight on November 7, 2004
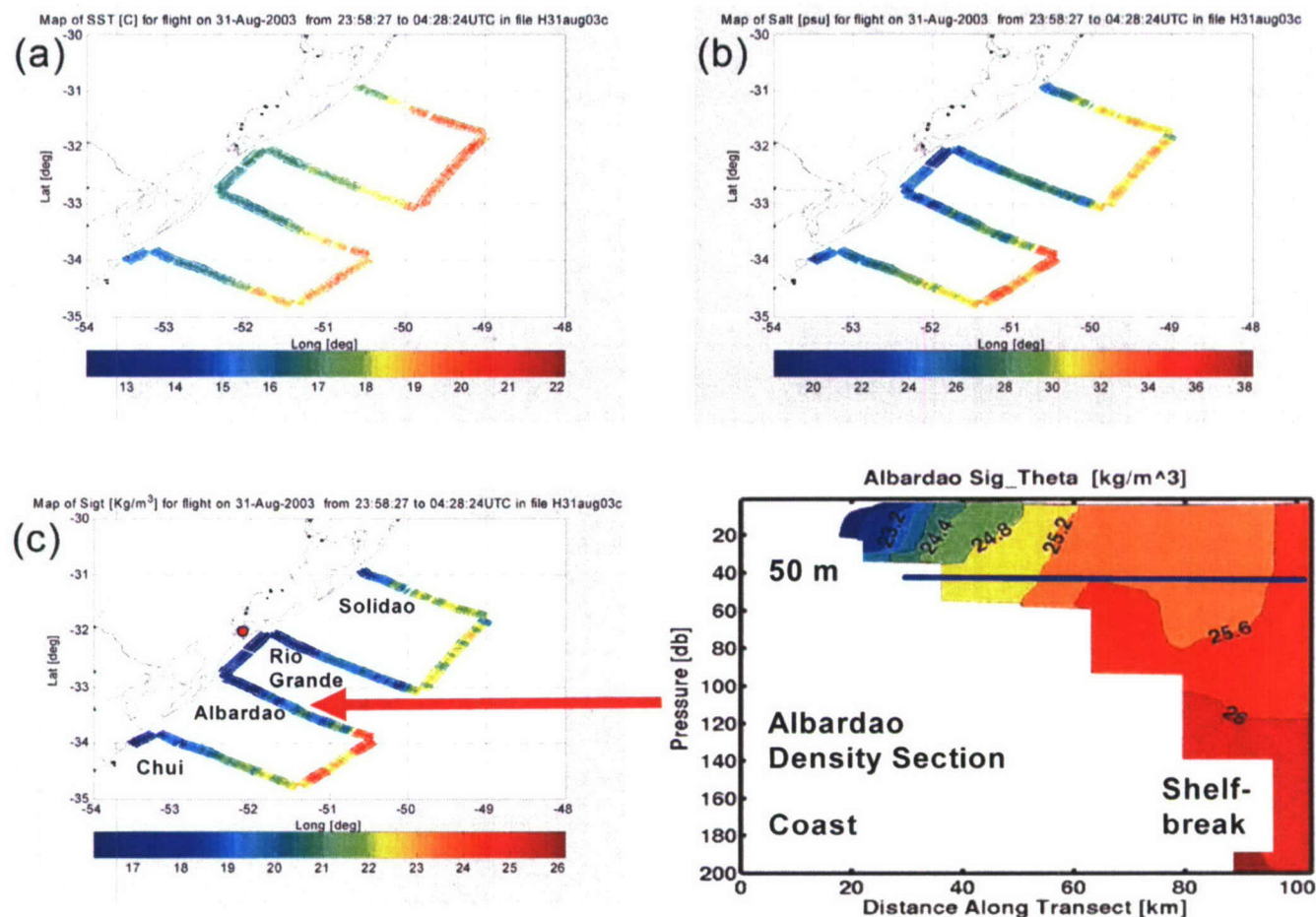
Fig. 13. STARRS survey spanning the continental shelf off Brazil that was flown in winter 2003, showing a portion of the Plata plume evident as a band of coastal water low in (a) SST, (b) SSS, and (c) SSD. (d) A ship survey conducted four days earlier along the Albardao showing a vertical section of D (σ_t).

[Fig. 12(a)] showed cool waters ($\sim$23 °C) near shore in the vicinity of the Mississippi Delta (29° S, 89° W) and at the western entrance into Mississippi Sound (30° S, 89° W) and warmer waters ($\sim$27 °C) seaward of these locations. This may be compared with the earlier summer flight on May 7, 2004. The summer SST survey [Fig. 12(b)] shows warmer temperatures ($\sim$26 °C) pervading the coastal domains of the delta and entrance to Mississippi Sound with a seaward extension into the western Mississippi Bight. These contrast with cooler offshore temperatures ($\sim$24 °C) south and east of the delta.

The winter and summer SSS maps [Fig. 12(c) and (d)] show similar patterns, with fresher waters near shore and more saline water well south and east of the delta. While the extreme salinity values are similar (5 and 30 psu), the area of freshwater influence is more extensive in the summer. However, during that season, a streamer of fresher water moved eastward and southward from the delta and, in subsequent surveys (not shown), entered the western end of NRL's "Slope to Shelf Energetics and Exchange Dynamics (SEED)" project mooring array, as confirmed by shipboard CTD profiles [37]. The salinities observed by STARRS agree with near-surface ($\sim$2-m depth) CTD measurements obtained inside the array, and the surface

temperatures are consistent with those from NOAA National Data Buoy Center data buoy 42 040 in the same area.

The winter and summer SSD distributions [Fig. 12(e) and (f)], respectively, closely follow the corresponding SSS distributions, which dominate the density variability, i.e., lower density water appears around the delta and in the entrance to the sound, with a seaward extension into Mississippi bight evident in the summer. However, the influence of the contrasting winter and summer SST distributions is evident, particularly around the delta and near the coast to the north, with SSD showing a weaker density gradient in these areas in the winter. This suggests that reinforcement in summer has intensified the density contrast in comparison with the compensating situation in winter. It is notable that, in contrast to winter, the density is lower within the mooring array in the summer despite SST's being cooler locally. This is associated with the lower salinities and is a further indication of salinity influence dominating temperature throughout the domain.

B. Density-Induced Geostrophic Current

The wintertime STARRS survey (Legs I–III) conducted off the Atlantic coast of South America showed the Plata plume
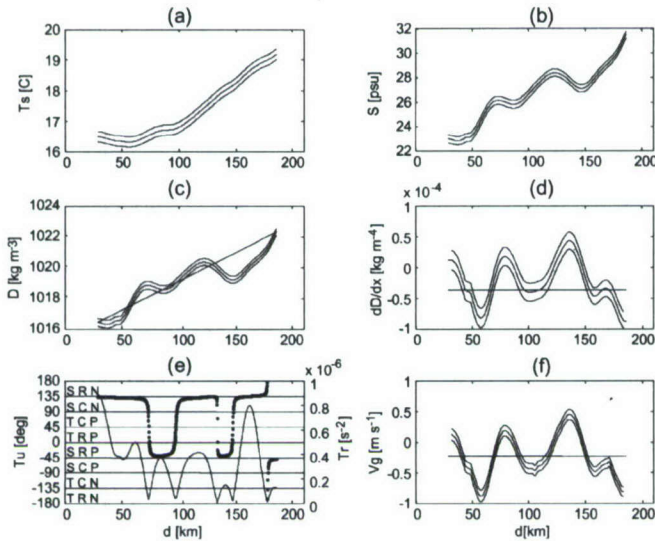
Fig. 14. STARRS data from the Albardao transect (shown in Fig. 13) plotted as an across-shelf profile through the Plata plume showing (a) SST, (b) SSS, (c) SSD, (d) horizontal density gradient, (e) Turner vector, and (f) geostrophic velocity at the base of a 50-m-deep surface layer.

extending from the Rio de la Plata entrance (latitude: $36°$ S) to north of Florianopolis ($28°$ S) along the Uruguayan and southern Brazilian continental shelf [38], [39]. Leg II of the survey showed cool fresh low-density water [Fig 13(a)–(c)] spread along the inner shelf, with warmer, more saline, and denser water seaward. The density is low (~ 17 σ_t) along the inner continental shelf and higher in the outer shelf and slope, increasing to ~ 23 σ_t in the northern part of the domain and to ~ 25 σ_t in the south, with a maximum across-shelf contrast of 8 σ_t units. This across-shelf SSD contrast is most readily seen in plots along the Albardao transect [Fig. 14]. As demonstrated for the Mississippi plume in the previous section, this high-density contrast resulted from the dominating effect of salinity due to the Plata river plume [Fig. 14(b)] acting in spite of, and partially compensated by, the generally cooler waters near the coast [Fig. 14(a)]. The salinities and densities are similar to those measured by the ship on the outer shelf four days earlier but are lower near shore. The STARRS temperatures are higher by an average of 2.5 °C, and the coastal salinities are lower and/or extend further seaward. These differences could be explained by the subsequent ship weather observations obtained admittedly $5°$ of latitude (~ 500 km) further north, which show that the air temperature warmed by 3 °C while the humidity rose by 10% and the winds shifting from south–southwest to west became less favorable for downwelling. In addition, STARRS measures SSS in the top few centimeters of the ocean, whereas the ship SSS measurements are from the bulk (~ 2-m depth). Thus, STARRS will likely observe fresher salinities in the presence of a thin or stratified buoyant plume.

A dimensional analysis of the along- and across-shelf momentum equations [38] showed that the Plata river plume, in winter, is approximately in semigeostrophic balance, with wind dominating bottom drag in the along-shelf (ageostrophic) bal-

ance and across-shelf pressure gradient balancing Coriolis force in the across-shelf (geostrophic) balance. We use this result to justify using the "thermal wind" term in (1) to investigate the effects of geostrophic shear in the near-surface waters over the shelf. The shipboard density vertical section obtained along the Albardao transect (Fig. 13(d), plotted from [40]) confirms the STARRS SSD observation of increasing density seaward across the shelf and particularly along the Albardao transect. This density section also demonstrates that the across-shelf density gradient is relatively uniform as a function of depth, down to a level of about 50 m, which corresponds to the inner portion of the continental shelf domain. The density sections along the Rio Grande and Solidao transects lying further north (not shown) exhibited a similar uniform horizontal density gradient and depth dependence. This structure likely exhibited weaker isopycnal tilts when the STARRS survey was undertaken four days later, in response to wind shifting to the west, but the relatively uniform pattern of horizontal and vertical density variations observed by the ship is likely to be a robust feature of the wintertime Plata plume. The corresponding STARRS horizontal SSD profile along the Albardao section [Fig. 14(c)], which was computed from the observed SST [Fig. 14(a)] and SSS [Fig. 14(b)], shows a spatially fluctuating, but generally increasing, density offshore (with the trend being marked by the solid straight line). The density gradient across the plume [Fig. 14(d)] was mostly compensating in T and S with S variations dominating the weak T gradient, except where the S gradient leveled off [Fig. 14(e)].

Based on the assumptions (previously justified) that the across-shelf momentum balance is geostrophic and that the horizontal density gradient is uniform as a function of depth within the specified depth range, we use the geostrophic theory in Section IV and Appendix C to determine the corresponding geostrophic velocity relative to the surface, at the base of this 50-m-deep layer. The along-shelf geostrophic velocity [Fig. 14], which was computed from the horizontal density gradient [Fig. 14(d)], after low-pass filtering density [Fig. 14(c)] using a Hanning filter with an effective cutoff wavelength of 30 km, fluctuates within the range of -1.0–0.5 m $\cdot$ s^{-1}. The geostrophic current at the base of the near-surface layer was strongest (southward), where the horizontal density gradient was dominated by salinity. It was reduced by the effects of density compensation in the middle and outer continental shelf (where the Turner angle approaches $90°$). It was reversed where reinforcement produced a negative density gradient [Fig. 14(e)], but the contributions of the T and S variations to the density gradient are weak in this area, as evidenced by the small Turner radius, and the actual density gradient is subject to greater uncertainty.

Filtering was performed to minimize the potential impact of small spatial scale fluctuations due to ageostrophic processes acting within the mixed layer over space and time (inertial or finer) scales that are too small to be significantly affected by the Earth's rotation. The filter cutoff wavelength was chosen based on estimates of the baroclinic Rossby radius L_R by Chelton et al. [41]. They mapped L_R globally using climatological T and S data in $1° \times 1°$ cells, with the result that $L_R \sim 30$ km off the South American Atlantic coast. Given the

complexity of the circulation in this region and the strong influence of river runoff on stratification, higher resolution estimates from representative current meter moorings or high-resolution shipboard acoustic Doppler and hydrographic measurements are needed to determine the space and time scales at which the geostrophic theory is valid over the continental shelf. As a more conservative estimate, which assumes a representative spatial scale corresponding to the width of the continental shelf, we also computed the spatial mean geostrophic velocity (based on the mean horizontal density gradient represented by the horizontal line in Fig. 14(d)). We found a mean value of -22 cm $\cdot$ s^{-1}, with the minus sign indicating southward flow at a depth of 50 m, relative to the surface. In doing this, we recognize that significant information on geostrophic current structure could reside at smaller scales.

As mentioned in Section IV, given an estimate of the barotropic surface current relative to a mean sea surface or a geoid, the baroclinic subsurface current computed here could be added to determine the total geostrophic current throughout the near-surface layer. Estimation of the barotropic component of the surface geostrophic current using these means has already been demonstrated by others [14]–[16] and [42] and lies outside our present scope. However, Strub *et al.* [15] discuss resolution scales for surface geostrophic currents obtained from altimetry, and Powell and Leben [43] have proposed a filter that optimizes the tradeoff between reducing altimeter noise and maintaining high spatial resolution. Strub *et al.*'s results suggest that surface geostrophic velocity Vs can be estimated from TOPEX altimeter data with a precision (rms difference) of about $7-8$ cm $\cdot$ s^{-1} using a 50-km-long "loess" filter and a gradient operator that spans 62 km. With this processing configuration, the cross-track velocities were found to resolve features with horizontal scales in the range of 50–80 km. The along-track spatial resolutions of satellite-borne L-band salinity mapping instruments (SMOS and Aquarius) over the deep ocean are expected to be comparable to those of the altimetric data [44]. This suggests the possibility of combining data from the altimeter and L-band radiometer systems to estimate absolute geostrophic currents near surface in deep ocean regions at spatial scales on the order of 100 km. Another possibility is suggested by a recent study by Isern-Fontanet *et al.* [17], which employed microwave SST data of ~50-km resolution to determine density-driven near-surface currents using an approximate SSS value and the QG theory. This theory is likely to be valid where mixed layer deepening or strong wind events, as in winter, produce a close relationship between surface density anomalies and the circulation in which they are embedded. The derivation of SSD from L-band microwave radiometry, as demonstrated here, could complement the QG theory and expand its domain of application to situations where knowledge of the SST alone is not sufficient to determine the SSD anomaly field. The QG method and our thermal-wind-based method share an advantage over the barotropic methods in that they relate the horizontal density structure to the vertical velocity structure and are capable of providing estimates of the vertical shear, and also the internal velocities, if the surface velocity is known.

VI. DISCUSSION

We have presented a simple algorithm for determining density from the microwave brightness and physical temperature of the sea surface based on the nonlinear Klein and Swift emissivity relation and the UNESCO SES [7], [11]. The nonlinearities result in a sensitivity of errors in D to errors in the observed Ts and Tb that significantly varies throughout the $Ts-Tb$ space. These errors were quantified for several idealized cases in which the effects of T and S either mutually compensate or reinforce one another in their effect on S. The analysis was extended to determine the expected precision and bias of SSD retrievals from the STARRS airborne radiometer system and from the SMOS and Aquarius salinity mapping satellites. We then applied a density compensation index, the "Turner vector" based on the density ratio [18], and the horizontal Turner angle [19] to give a compact representation of both the significance and influence of S and T on D and showed that errors in retrieving horizontal density gradients depended on whether the S and T contributions were mutually compensating or reinforcing.

We used the SSD algorithm to retrieve SSD information from SST and SSS observations obtained from the STARRS airborne IR and microwave radiometers, with sufficient precision for several practical oceanographic applications. These included mapping the surface density of two major river plumes spanning the continental shelf, determining the relative compensation or reinforcement effects of S and T on D, in the Mississippi plume during summer and winter, and estimating surface geostrophic shear and subsurface geostrophic current in the Plata plume during winter.

The Mississippi and Plata river plumes showed evidence of density compensation and density reinforcement, associated with cool or warm seasons having offshore temperature gradients of the opposite sign. For the Mississippi River plume, the SST and SSS were either correlated (winter) or anticorrelated (summer) and alternately showed compensation or reinforcement, respectively. In contrast to the Mississippi plume, the Plata plume was of larger scale, and in winter, it formed a persistent buoyant coastal current that propagated northward, under the combined influence of Earth's rotation and southerly winds.

The density gradient across the Plata plume was mostly compensating in T and S with S variations dominating the weak T gradient, except where the S gradient leveled off. Since, under these conditions, the buoyant plume exhibited a semigeostrophic momentum balance, it was possible to use the across-shelf horizontal density gradient to compute the geostrophic current shear at the surface. Subject to appropriate assumptions, the subsurface geostrophic current due to the horizontal density gradient was inferred. The assumptions, which allow for an arbitrary variation of density in the horizontal direction and linear variation in the vertical direction are not overly restrictive, and the linear constraint could be relaxed when more information is available on the vertical density variation. The current was strongest (southward) where the horizontal density gradient was dominated by salinity. It was reduced by the effects of density compensation in the middle

and outer continental shelf and reversed where reinforcement produced a negative density gradient.

VII. CONCLUSION

Based on the foregoing algorithm development, assessments of algorithm performance, and our experience with STARRS, the determination of SSD from satellite IR and microwave observations of SST and SSS appears feasible. More work is needed to identify the likely error levels (both accuracy and precision) for SSD determined from the satellite salinity mapping technology, under conditions that will be encountered at the surface of the deep ocean. The estimation of geostrophic currents associated with horizontal density gradients, which could be added to altimetric surface geostrophic current velocity estimates to determine the near-surface geostrophic current profile, can also be envisaged under appropriate assumptions and in specific geographic regions.

This paper has focused on the retrieval of SSD and geostrophic shear from airborne radiometer systems in coastal regions subject to buoyancy-driven coastal currents. Future studies will focus on determining the feasibility of the SSD and geostrophic shear retrieval from the SMOS and Aquarius satellite systems in specific regions and seasons subject to moderate to strong buoyancy contrasts, such as western boundary currents, and, more generally, at the margins of the synoptic and basin scale where the signals are likely weaker but broader in the horizontal scale.

Our error estimates suggest that SSD can be determined in temperate and tropical climates at approximately equal levels of precision and accuracy of $\sim$0.75 and 0.25 kg $\cdot$ m^{-3} for SMOS and Aquarius, respectively, with temporal but no spatial averaging, at resolutions of $\sim$100 km. If the postlaunch error levels for satellite determinations of both surface density SSD and vertical shear of the geostrophic velocity dV_g/dz prove to be acceptable, density products derived from these satellites could be developed and used in a number of ways. For example, the SSD information could be directly assimilated into numerical hydrodynamic models as an alternative to the current practice of independently specifying surface temperature and salinity. This might have computational advantages for certain types of models, specifically those that were set up to investigate dynamical issues. Identical twin experiments could be performed to determine the relative advantages of assimilating either SST and SSS or SSD in such models. The products could be used independently of the models, or they could exhibit a weak dependence on them; models and *in situ* mooring data could be used to determine the validity of the assumptions of geostrophy and uniformity of subsurface horizontal density gradient in specific regions. In either case, the production of an operational algorithm that generates estimates of both SSD and $dV_g(z)/dz$ could be useful in combination with estimates of SSH and surface geostrophic current Ve available from satellite altimeters. This suggests that existing products such as OSCAR [16], [45], which account for both geostrophic and Ekman effects to estimate surface drift, could be upgraded to take advantage of the baroclinic shear deduced from the salinity mapping satellites to project surface current estimates into the subsurface.

APPENDIX A
INSTRUMENTATION AND DATA PROCESSING

1) Instrumentation: STARRS (Fig. 11) is an airborne radiometer system built for NRL to map SSS in estuaries and marginal seas. It is flown beneath a twin-engined aircraft [Fig. 11(a)] and comprises L- and C-band microwave radiometers and an IR radiometer [Fig. 11(b)] with an integrated Global Positioning System (GPS) receiver and fiber-optic gyro [30], [39], [46]. Its primary purpose is to map coastal SSS, SST, and SSR. The L-band radiometer, which is used to map SSS, is a multibeam system sensing natural microwave emission from the sea surface within a 24-MHz-wide protected band centered at a frequency of 1.413 GHz. It has a brightness temperature sensitivity of 0.35 K at a sampling interval of 2 s. This is equivalent to 0.52 K at 1 s and can be reduced to 0.28 and 0.21 K by averaging over 12 and 24 s, respectively. Due to some sample autocorrelation, this reduction is less than Gaussian (which scales as $1/\sqrt{N}$, where N is the number of samples averaged). The six antenna beams, each with 15° half-power beam width, point downward and to either side of the aircraft at incidence angles of $\pm$7°, 22°, and 38° [Fig. 11(c)]. The C-band radiometer, which can sense both SSR and SST, has a single 20° wide beam directly pointing beneath the aircraft (nadir viewing). It senses natural emission within six channels, at 5.2, 5.6, 5.9, 6.2, 6.6, and 7.1 GHz. The nadir-viewing IR radiometer measures SST independently from thermal emission in the 8–14-μm and 9.6–11.5-μm bands. In contrast to the L- and C-band radiometers, it cannot penetrate clouds, so gaps in the IR observations are filled by interpolation. The GPS and gyro provide Coordinated Universal Time (UTC) time and position, and aircraft attitude, respectively. For typical aircraft altitudes of 2600 m, the six L-band beams have footprints with a width of 700–1100 m and a swath of 5.2-km.

STARRS instruments are calibrated before and after each mission. The IR radiometer is calibrated at various steps spanning the observational temperature range using a blackbody target immersed in a temperature controlled water bath. The L- and C-band instruments are more difficult to calibrate due to their large antenna size and wide Tb range. This is done first in the laboratory by observing a room temperature ($\sim$300 K) target comprising a microwave absorbing mat, with its temperature monitored to provide a "warm" calibration point. The instrument is then set up outside at night (avoiding solar radiation) to observe the brightness temperature of the cold sky ($\sim$8 K), which provides the "cold" calibration point. The sky temperature is determined by the constant cosmic background plus galactic emissions in the field of view and is augmented by atmospheric O_2 emission and attenuated by atmospheric absorption. Instrument stability is assured by thermal regulation and the measurement of internal temperatures of key components, including the antennas, and hot and cold calibration reference targets. Calibration involves regressing the observed brightness temperature of the external and internal

targets against the known target brightness temperatures while taking into account the internal physical temperatures of the components and reference noise sources to obtain a multivariate calibration curve. Internal sampling and processing operations minimize the effects of instrument drift and gain variations and temporally average the data to maximize sensitivity [30]. During operational deployment, the internal calibration targets are sampled at regular intervals and used to correct the interspersed Tb observations of the seawater surface. These vary over $\sim 100-130$ K, depending on the incidence angle and allowing for the various factors mentioned in Section II.

2) Data Acquisition and Processing: Surveys of the Mississippi River plume using STARRS were conducted in early boreal summer during May 2–8 and in early winter during November 4–17, 2004. The flights coincided with *in situ* shipboard sampling of T and S, and were bracketed by the deployment of an extensive mooring array spanning the continental shelf break east of the Mississippi Delta, as part of NRL's SEED experiment. Surveys of the Plata River plume were conducted in the austral winter between August 19 and September 5, 2003 and in summer between January 30 and February 10, 2004. The flights spanned the continental shelf and extended from northern Argentina (latitude: 38° S) to Southern Brazil (latitude: 27° S), which is a distance of some 1200 km, including the outflow from the Rio de la Plata estuary and Patos Lagoon (see [39] for a more detailed description of the mission and salinity survey results). The flights reported here were performed in the line-transect mode with tracks separated by gaps, in contrast to the mapping mode, which gives complete spatial coverage. Altitudes were chosen to optimize the sampling subject to operational constraints, such as aircraft range (duration) and cloud cover.

The calibrated STARRS thermal IR radiometer data were used to determine SST by using a dual-window algorithm with corrections for the effects of the intervening water vapor obtained from estimates of precipitable water vapor. The latter water vapor was estimated using surface measurements of wet and dry bulb temperature (or dew point) from meteorological buoys (during the SEED surveys) or the ship's weather station (during Plata), and an assumed exponential falloff in water vapor concentration with height [47], with a 22-km scale height [48, p. 171]. The calibrated L-band brightness temperatures were first edited to remove anomalous pixels due to the presence of land in the field of view or aircraft maneuvers, and data obtained from beam 3R during the May 2004 survey were omitted due to an instrument noise problem affecting only that beam, which has since been remedied. The remaining Tb values were corrected for reflected atmospheric O_2 and extraterrestrial (cosmic and galactic) emission, atmospheric absorption, and wind-induced roughness and then converted to SSS by empirical inversion of the KS77 relation. The roughness correction was performed using the Camps *et al.* [33] empirical formula using representative wind speeds from buoy and/or ship anemometers adjusted to the standard meteorological height (10 m). The KS77 algorithm accounted for the effects of SST, polarization, and beam incidence angle (coupled with aircraft pitch and roll) on the retrieved SSS. An additional empirical roll bias correction was applied to

correct across-track brightness temperature differences: 1.5° in the November 2004 data (SEED) and 0.5° in the August (Plata) data. These differences were likely due to gyro initialization errors since subsequent gyro replacement eliminated this error. Residual across-track differences evident in the November 2004 data are likely due to small beam-to-beam calibration biases that are consistent with the known instrument Tb calibration precision ($\sim$0.7 K).

APPENDIX B
TURNER VECTOR

The density ratio defines the relative contribution of thermal and haline gradients and associated anomalies to the observed density gradients. It is defined as [18]

$$R_\rho = \frac{\alpha dT/dx}{\beta dS/dx} \tag{3}$$

where α and β are the coefficients of thermal expansion and haline contraction, respectively. These are defined as [13, p. 254]

$$\alpha \equiv -\frac{1}{D}\left(\frac{\partial D}{\partial T}\right)_{S,P} \qquad \beta \equiv \frac{1}{D}\left(\frac{\partial D}{\partial S}\right)_{T,P}. \tag{4}$$

In (3), we express the anomalies as spatial gradients in T and S as a function of horizontal distance x offshore, in contrast to the usual representation of R_ρ used in fine-structure studies (in which gravity plays a key role), in terms of vertical derivatives in depth z.

Using the definition of the total derivative (on the left) with respect to partial derivatives (on the right), the horizontal density gradient is

$$dD/dx = \left(\frac{\partial D}{\partial T}\right)_{T,P}\left(\frac{\partial T}{\partial x}\right) + \left(\frac{\partial D}{\partial S}\right)_{T,P}\left(\frac{\partial S}{\partial x}\right). \tag{5}$$

This can be expressed in terms of a nondimensional density and the preceding quantities (4) as

$$\frac{1}{D}\frac{dD}{dx} = \alpha\frac{dT}{dx} - \beta\frac{dS}{dx}. \tag{6}$$

If S and T variations are both significant (in the sense defined here), $dD/dx = 0$ implies perfect compensation, whereas if dD/dx is large, either reinforcement is occurring or one of T and S is strongly dominating D. To find out whether compensation or reinforcement is occurring and which of T or S dominates the density gradient, we can examine the sign of the density ratio R_ρ and its magnitude, or absolute value $|R_\rho|$ relative to unity. If $R_\rho > 0$, T and S compensate in their effect on D, whereas if $R_\rho < 0$, they reinforce their effect on D. If $|R_\rho| > 1$, T effects dominate those of S, and if $|R_\rho| < 1$, S dominates T. To determine the utility of this approach, we plotted R_ρ and $|R_\rho|$ for the arbitrary density profile of Fig. 4(c) and found that reinforcement occurs most of the way across the shelf, whereas compensation occurs at the outer end. In addition, S dominated T everywhere, except in a narrow band at $D = 40$ km, where R_ρ changed sign.

As previously implied, if $dD/dx \approx 0$, this could be due to perfect compensation of T and S, but this condition could also be met if T and S show no significant variation ($dT/dx \approx 0$, $dS/dx \approx 0$). In this case, R_ρ is a ratio of two very small numbers subject to noise and is thus poorly defined. To reveal such cases, we need an indicator of the absolute strength of the corresponding variations in T and S. An inconvenient singularity also arises in R_ρ when $dS/dx = 0$, causing it to become infinite. An approach that both avoids the singularities and properly represents the four combinations arising from each pair of compensation and dominance states was proposed by [18] in the form of a four-quadrant arctangent "Turner angle" Tu expressed in degrees, which is related to the density ratio by

$$R_\rho = -\tan(Tu + 45). \tag{7}$$

A simple four-quadrant arctangent of the terms in the density ratio would serve our purposes for studies of horizontal density variations. However, we chose to adopt the slightly more esoteric Turner angle (with its 45° offset) for consistency with studies of double diffusive processes, which focus on vertical T and S gradients.

Ruddick [18] defines Tu in terms of Cartesian coordinates corresponding to appropriately signed values of the density ratio numerator and denominator, i.e.,

$$\left[N_S^2 = \pm g\beta \frac{dS}{dx}, N_T^2 = \pm g\alpha \frac{dT}{dx} \right]. \tag{8}$$

In his notation, the signs are chosen, so positive (N_S^2, N_T^2) corresponds to gravitationally stable S and T stratification ($d\rho/dz > 0$, with z pointing down). For application to horizontal variations [19], for which we substitute the x for z, gravity is unimportant, and the signs merely determine the x-direction, which is considered to represent a positive density gradient. We choose the signs in (8) to be positive and negative for the first and second terms, respectively, so that a positive density gradient $d\rho/dx > 0$ corresponds to D and S increasing, and T decreasing, in the x-direction. Ruddick's use of the acceleration due to gravity g and exponent 2 (which is symbolic and not mathematical) is evidently linked to the definition of the square of the Brunt-Vaisalla frequency in terms of vertical density gradient, which does not concern us here either.

The Turner angle, which is defined in these terms using the "atan2" label of the FORTRAN and MATLAB (The Mathworks Inc.) syntax to denote the four-quadrant arctangent function, is

$$Tu = \arctan 2 \left(N_T^2 - N_S^2, N_S^2 + N_T^2 \right). \tag{9}$$

As an indication of the combined strength of the S and T gradients influencing D (regardless of whether they are compensating or reinforcing and which dominates), we further define the Turner "radius." The radius, with units of square frequency, represents the combined magnitudes of the coordinates defined in (8), i.e.,

$$Tr = \sqrt{\left(N_S^2\right)^2 + \left(N_T^2\right)^2}. \tag{10}$$

The resulting vector (Tr, Tu), which, adapting Ruddick's terminology, we term the "Turner vector" can be plotted either in point form on a polar coordinate frame or in component form, as a function of the space dimension in a Cartesian frame (see Figs. 1 and 2).

In our polar representation (e.g., Fig. 8), which can be obtained from that of Ruddick [18, Fig. 1], by rotating his disc out of plane about its $Tu = 0$ axis ($R_\rho = -1$ diagonal), Turner angles falling within the two right-side quadrants correspond to positive horizontal density gradients, whereas those occupying the left-side quadrants represent negative density gradients. In quadrants 1 and 3, T dominates S, whereas, in quadrants 2 and 4, S dominates T. If these four quadrants of the circle are each subdivided to form eight 45° sectors numbered counterclockwise from the zero-degree line at the right, then sectors 1, 4, 5, and 8 represent T and S reinforcement, and sectors 2, 3, 6, and 7 represent T and S compensation. Reinforcement is strongest in the 0° and 180° directions, whereas compensation is most perfect in the ±90° directions. Finally, the radial distance from the center of the circle represents the combined strength of the T and S gradients. In studies of vertical gradients, the right- and left-hand quadrants represent stable and unstable density stratification, respectively, whereas sectors 2 and 7 represent salt fingering and double diffusive activity, respectively. However, neither characteristic is relevant when examining horizontal gradients.

APPENDIX C
DERIVING GEOSTROPHIC CURRENTS

Geostrophic current is determined by the following simplified horizontal momentum balance equation (see standard texts such as [49] or [50] for derivations). A right-handed Cartesian coordinate system is used, with the vertical z-axis positive above the mean sea surface. For momentum balance in the x-axis direction (oriented across-shelf and positive offshore in our STARRS applications), the acceleration due to the Coriolis force (at left) is canceled by that generated by the pressure gradient force (at right), i.e.,

$$fV_g = \frac{1}{D(x)} \frac{dP}{dx}. \tag{11}$$

Here, $f = 2\Omega \sin(\eta)$ is the Coriolis parameter, which is positive/negative in the Northern/Southern Hemisphere, Ω is the Earth's rotation rate (in radians per second), η is the latitude, and V_g is the speed of the geostrophic current. This flows in the y-axis direction perpendicular to the horizontal pressure gradient (with high pressure on the right in the northern hemisphere). Following the Boussinesq approximation, the density, which modifies pressure gradient dP/dx, is represented by a reference density D_0, which is here chosen to be the observed surface density $D(x)$.

The pressure gradient can arise from external (sea level) or internal (density) differences. The vertical hydrostatic approximation to the vertical momentum balance provides the relationship between the density and pressure needed to

determine the geostrophic current from density observations in the ocean, i.e.,

$$dP/dz = -gD(x, z) \tag{12}$$

where g is the acceleration due to gravity, which is assumed to be constant over the depths and horizontal locations of interest here.

To maintain accuracy when computing P from (12), the more general position- and depth-dependent form of the density function $D(x, z)$ is retained, consistent with the Boussinesq approximation. Given the density variation with depth, (12) can be integrated to give pressure at any level z. We fix $z = 0$ at the mean sea level but define $z = \xi(x)$ at the actual surface. This allows for small vertical excursions, or more significantly for geostrophic balance, larger scale tilt about the mean, which may horizontally vary along x, i.e.,

$$P(x, z) = P(\xi(x)) + g \int_z^{\xi(x)} D(x, z)dz \tag{13}$$

where $P(\xi(x))$ is the surface (atmospheric) pressure.

If we assume that density varies arbitrarily in x and linearly in z, we can write

$$D(x, z) = D(x)(1 - z/a) \tag{14}$$

where a is the scale depth for the vertical density variation, which is empirically estimated here. Substituting this expression into (13) and the resulting $P(x, z)$ relation into (11) yields a form of the "thermal wind" equation, which is so called in meteorology because the temperature effect on density dominates vertical variations in geostrophic wind, i.e.,

$$V_g(z) = \frac{g}{fD(x)} \frac{d}{dx} \int_z^{\xi(x)} D(x)(1 - z/a)dz. \tag{15}$$

Moving $D(x)$ outside the integral and then integrating the depth-dependent part between limits, we get

$$V_g(z) = \frac{g}{fD(x)} \frac{d}{dx} \left[D(x) \left(\xi(x) - \frac{\xi(x)^2}{2a} - z + \frac{z^2}{2a} \right) \right]. \tag{16}$$

Differentiation of the product, allowing for the x-dependence of surface height, leads to

$$V_g(z) = \frac{g}{fD(x)} \left\{ D(x) \left(\frac{d\xi(x)}{dx} - \frac{\xi(x)}{a} \frac{d\xi(x)}{dx} \right) + \left[\frac{dD(x)}{dx} \left(\xi(x) - \frac{\xi(x)^2}{2a} - z + \frac{z^2}{2a} \right) \right] \right\}. \tag{17}$$

Here, all fractions involving both $\xi(x)$ and a can be neglected, and $\xi(x)$ is dominated by z for all depths of practical interest. With this and some further simplification, we get

$$V_g(z) = \frac{g}{fD(x)} \left\{ D(x) \frac{d\xi(x)}{dx} - \frac{dD(x)}{dx} z \left(1 - \frac{z}{2a} \right) \right\}. \tag{18}$$

If a is known with some certainty, the full expression (18) can be used, but substituting a representative surface density of 1015 σ_t with an increase of 10 σ_t over 100-m depth into (14) gives $a \sim 10$ km, so for depths on the order of 100 m, e.g., over the continental shelf, the term involving z/a can be neglected with a velocity error on the order of 1%. With this simplification, we have

$$V_g(z) = \frac{g}{f} \frac{d\xi(x)}{dx} - \frac{gz}{fD(x)} \frac{dD(x)}{dx}. \tag{19}$$

In this final expression for the total geostrophic velocity at depth z, the first term on the RHS can be recognized as the surface geostrophic velocity associated with the sea surface slope, while the second is the internal velocity relative to the surface associated with the horizontal density gradient.

REFERENCES

[1] D. M. Burrage, M. L. Heron, J. M. Hacker, T. C. Stieglitz, C. R. Steinberg, and A. Prytz, "Evolution and dynamics of tropical river plumes in the Great Barrier Reef: An integrated remote sensing and in situ study," *J. Geophys. Res.*, vol. 107, no. C12, pp. SRF 17-1–SRF 17-22, 2002, DOI:10.1029/2001JC001024.

[2] D. M. Burrage, M. L. Heron, J. M. Hacker, J. L. Miller, T. C. Stieglitz, C. R. Steinberg, and A. Prytz, "Structure and influence of tropical river plumes in the Great Barrier Reef: Application and performance of an airborne sea surface salinity mapping system," *Remote Sens. Environ.*, vol. 85, no. 2, pp. 204–220, May 2003.

[3] Y. H. Kerr, P. Waldteufel, J.-P. Wigneron, J. Martinuzzi, J. Font, and M. Berger, "Soil moisture retrieval from space: The Soil Moisture and Ocean Salinity (SMOS) mission," *IEEE Trans. Geosci. Remote Sens.*, vol. 39, no. 8, pp. 1729–1735, Aug. 2001.

[4] P. Silvestrin, M. Berger, Y. H. Kerr, and J. Font, "ESA's second earth explorer opportunity mission: The Soil Moisture and Ocean Salinity Mission—SMOS," *IEEE Geosci. Remote Sens. Soc. Newslett.*, no. 118, pp. 11–14, Mar. 2001.

[5] J. Font, G. S. E. Lagerloef, D. M. Le Vine, A. Camps, and O.-Z. Zanife, "The determination of surface salinity with the European SMOS space mission," *IEEE Trans. Geosci. Remote Sens.*, vol. 42, no. 10, pp. 2196–2205, Oct. 2004.

[6] D. M. Le Vine, G. S. E. Lagerloef, S. Yueh, F. Pellerano, E. Dinnat, and F. Wentz, "Aquarius mission technical overview," in *Proc. IGARSS*, Denver, CO, Jul. 31–Aug. 4, 2006, pp. 1678–1680.

[7] L. Klein and C. Swift, "An improved model for the dielectric constant of sea water at microwave frequencies," *IEEE Trans. Antennas Propag.*, vol. AP-25, no. 1, pp. 104–111, Jan. 1977.

[8] W. Ellison, A. Balana, G. Delbos, K. Lamkaouchi, L. Eymard, C. Guillou, and C. Prigent, "New permittivity measurements of sea water," *Radio Sci.*, vol. 33, no. 3, pp. 639–648, 1998.

[9] C. Gabarro, M. Vall-llosera, J. Font, and A. Camps, "Determination of sea surface salinity and wind speed by L-band microwave radiometry from a fixed platform," *Int. J. Remote Sens.*, vol. 25, no. 1, pp. 111–128, Jan. 2004.

[10] A. Camps, J. Font, M. Vall-llosera, R. Villarino, C. Gabarro, L. Enrique, J. Miranda, I. Corbella, N. Duffo, F. Torres, S. Blanch, A. Aguasca, and R. Sabia, "From the determination of sea emissivity to the retrieval of salinity: Recent contributions to the SMOS mission from the UPC and ICM," in *Proc. IGARSS*, Denver, CO, Jul. 31–Aug. 2006, pp. 1697–1701.

[11] UNESCO, "Algorithms for computation of fundamental properties of seawater, " *Technical Papers in Marine Science, #44*, UNESCO Division Marine Sci., Paris, France, 1983.

[12] D. M. Burrage and R. W. Garvine, "Summertime hydrography at the shelfbreak front in the middle atlantic bight," *J. Phys. Oceanogr.*, vol. 18, no. 10, pp. 1309–1319, Oct. 1988.

[13] J. S. Turner, *Buoyancy Effects in Fluids*. Cambridge, U.K.: Cambridge Univ. Press, 1973.

[14] R. Morrow, R. Coleman, J. Church, and D. Chelton, "Surface eddy momentum flux and velocity variances in the southern ocean from Geosat altimetry," *J. Phys. Oceanogr.*, vol. 24, no. 10, pp. 2050–2071, Oct. 1994.

[15] P. T. Strub, T. K. Chereskin, P. P. Niller, C. James, and M. D. Levine, "Altimeter-derived variability of surface velocities in the California Current System—Part 1: Evaluation of TOPEX altimeter velocity resolution," *J. Geophys. Res.*, vol. 102, no. C6, pp. 12 727–12 748, 1997.

[16] G. S. E. Lagerloef, G. Mitchum, R. Lukas, and P. Niiler, "Tropical Pacific near-surface currents estimated from altimeter, wind and drifter data," *J. Geophys. Res.*, vol. 104, no. C10, pp. 23 313–23 326, 1999.

[17] J. Isern-Fontanet, B. Chapron, G. Lapeyre, and P. Klein, "Potential use of microwave sea surface temperatures for the estimation of ocean currents," *Geophys. Res. Lett.*, vol. 33, no. 24, L24 608, 2006, DOI:10.1029/2006GL027801.

[18] B. Ruddick, "A practical indicator of the stability of the water column to double-diffusive activity," *Deep-Sea Res., Part A*, vol. 30, no. 10A, pp. 1105–1107, Oct. 1983.

[19] G. L. Johnson, "Generation and initial evolution of a mode water θ-S anomaly," *J. Phys. Oceanogr.*, vol. 36, no. 4, pp. 739–751, 2006.

[20] R. Debye, *Polar Molecules*. New York: Chemical Catalog, 1929.

[21] E. Lewis, "The practical salinity scale 1978 and its antecedents," *IEEE J. Ocean. Eng.*, vol. OE-5, no. 1, pp. 3–8, Jan. 1980.

[22] S. Blanch and A. Aguasca, "Seawater dielectric permittivity model from measurements at L-band," in *Proc. IGARSS*, Anchorage, AK, Sep. 2004, pp. 20–24.

[23] W. J. Wilson, S. H. Yueh, S. J. Dinardo, and F. K. Li, "High-stability L-band radiometer measurements of saltwater," *IEEE Trans. Geosci. Remote Sens.*, vol. 42, no. 9, pp. 1829–1835, Sep. 2004.

[24] F. J. Millero and A. Poisson, "International one-atmosphere equation of state of seawater," *Deep-Sea Res.*, vol. 28, pp. 625–629, 1981.

[25] D. M. Burrage, M. L. Heron, and M. Goodberlet, "Simulating passive microwave radiometer designs using SIMULINK," *Simulation*, vol. 78, no. 1, pp. 36–55, 2002.

[26] J. Boutin, P. Waldteufel, N. Martin, G. Caudal, and E. Dinnat, "Surface salinity retrieved from SMOS measurements over the global ocean: Imprecisions due to sea surface roughness and temperature uncertainties," *J. Atmos. Ocean. Technol.*, vol. 21, no. 9, pp. 1432–1447, Sep. 2004.

[27] A. Camps, M. Vall-llossera, L. Batres, F. Torres, N. Duffo, and I. Corbella, "Retrieving sea surface salinity with multiangular L-band brightness temperatures: Improvement by spatiotemporal averaging,"*Radio Sci.*, vol. 40, no. 2, 13, Mar. 2005, DOI: 10.1029/2004RS003040.

[28] R. Sabia, A. Camps, N. Reul, and M. Vall-llossera, "Impact on sea surface salinity retrieval of multi-source auxiliary data within the SMOS mission," in *Proc. IGARRS*, 2005, vol. 1, pp. 284–287.

[29] R. Sabia, A. Camps, M. Vall-llossera, and N. Reul, "Retrieved sea surface salinity dependence on multi-source auxiliary data within the SMOS mission," in *Proc. IEEE MicroRad*, 2006, pp. 109–114.

[30] D. M. Burrage, J. C. Wesson, M. A. Goodberlet, and J. L. Miller, "Optimizing performance of a microwave salinity mapper: STARRS L-band radiometer enhancement," *J. Atmos. Ocean. Technol.*, 2008, to be published.

[31] G. S. E. Lagerloef, "Aquarius/SAC-D mission status—Sea surface salinity: Understanding the interactions between the global water cycle, ocean circulation and climate," presented at the 5th Int. SMOS Workshop: ESA-ESRIN, Frascati, Italy, Nov. 29–Dec. 1, 2004. [Online]. Available: http://earth.esa.int/workshops/smos04/presentations/SMOS_SW5_Aquarius_status.pdf

[32] G. S. E. Lagerloef, "Aquarius/SAC-D mission overview—Sea surface salinity: Understanding the interactions between the global water cycle, ocean circulation and climate," presented at the Aquarius/SAC-D-SMOS-HYDROS Joint Science Workshop, Miami, FL, Apr. 20–22, 2004. [Online]. Available: http://www.esr.org/mainfiles/pres_list/pres_files/aquarius/JSW_04/JSW_talk_04.pdf

[33] A. Camps, R. Villarino, L. Enrique, M. Vall-LLossera, J. Miranda, and I. Corbella, "Sea surface emissivity at L-band: Derived dependence with incidence and azimuth angles," in *Proc. ESA SP-525 First Results Workshop EuroSTARRS WISE LOSAC*, Cesbio, France, Nov. 4–6, 2002, pp. 105–116.

[34] E. J. Kearns, J. A. Hanafin, R. H. Evans, P. J. Minnett, and O. B. Brown, "An independent assessment of Pathfinder AVHRR sea surface temperature accuracy using the Marine Atmosphere Emitted Radiance Interferometer (MAERI)," *Bull. Amer. Meteorol. Soc.*, vol. 81, no. 7, pp. 1525–1536, 2000.

[35] F. Sakaida, S. Takahashi, T. Shimada, Y. Kawai, H. Kawamura, K. Hosoda, and L. Guan, "The production of the new generation sea surface temperature (NGSST-O Ver.1.0) in Tohoku University," in *Proc. IGARSS*, 2005, vol. 4, pp. 2602–2605.

[36] N. Ebuchi, "Intercomparison of wind speeds observed by AMSR and Sea Winds on ADEOS-II," in *Proc. IGARSS*, 2005, vol. 5, pp. 3314–3317.

[37] J. Wesson, D. Burrage, J. Miller, W. Teague, and D.-S. Ko, "Airborne salinity mapper measurements in the Gulf of Mexico nearshore and shelf region," presented at the IEEE Int. Geoscience and Remote Sensing Symp. (IGARSS), Denver, CO, Jul. 31–Aug. 4, 2006.

[38] D. M. Burrage, J. Wesson, C. Martínez, T. Pérez, O. Moller Jr., and A. Piola, "Patos Lagoon outflow within the Rio de la Plata plume using an airborne salinity mapper: Observing an embedded plume," *Cont. Shelf Res.*, 2008, to be published.

[39] T. Pérez, J. Wesson, and D. Burrage, "Airborne remote sensing of the Rio de la Plata Plume using a microwave radiometer system," *Sea Technol.*, vol. 47, no. 9, pp. 31–34, Sep. 2006.

[40] A. R. Piola, O. O. Möller, Jr., and J. H. Muelbert, *The Plata Winter Cruise 2003, Cruise Report*, Oct. 10, 2003.

[41] D. B. Chelton, R. A. DeSzoeke, and M. G. Schlax, "Geographical variability of the first baroclinic Rossby radius of deformation," *J. Phys. Oceanogr.*, vol. 28, no. 3, pp. 433–460, Mar. 1998.

[42] O. Leeuwenburgh and D. Stammer, "Uncertainties in altimetry-based velocity estimates," *J. Geophys. Res*, vol. 107, no. C10, pp. 39-1–39-16, 2002, DOI:10.1029/2001JC000937.

[43] B. S. Powell and R. R. Leben, "An optimal filter for geostrophic mesoscale currents from along-track satellite altimetry," *J. Atmos. Ocean. Technol.*, vol. 21, no. 10, pp. 1633–1642, Oct. 2004.

[44] G. S. E. Lagerloef, C. T. Swift, and D. M. Le Vine, "Sea surface salinity: The next remote sensing challenge," *Oceanography*, vol. 8, no. 2, pp. 44–50, 1995.

[45] F. Bonjean and G. S. E. Lagerloef, "Diagnostic model and analysis of the surface currents in the tropical Pacific Ocean," *J. Phys. Oceanogr.*, vol. 32, no. 10, pp. 2938–2954, Oct. 2002.

[46] J. L. Miller and M. Goodberlet, "Development and application of STARRS—A next generation airborne salinity imager," *Int. J. Remote Sens.*, vol. 25, no. 7/8, pp. 1319–1324, 2004.

[47] S. E. Tuller, "World distribution of mean monthly and annual precipitable water," *Mon. Weather Rev.*, vol. 96, no. 11, pp. 785–797, Nov. 1968.

[48] J. V. Hann, *Lehrbuch der Meteorologie [Compendium of Meteorology], Zwiete, Neubearbeitete Auflage (translated Second Revised Edition)*. Leipzig, Germany: Chr. Herm. Tauchnitz, 1906, p. 642. (see p. 171), (cited in [47], original not seen).

[49] S. Pond and G. Pickard, *Introductory Dynamic Oceanography*, 2nd ed. New York: Pergamon, 1983, p. 329.

[50] R. H. Stewart, *Introduction to Physical Oceanography*. College Station, TX: Dept. Oceaonography, Texas A&M Univ., Sep. 2006, [Online]. Available:http://oceanworld.tamu.edu/resources/ocng_textbook/contents.html

Derek Burrage received the B.Sc. degree in geophysics from the University of Melbourne, Melbourne, Australia, in 1971, the M.Env.Sc. degree from Monash University, Clayton, Australia, in 1978, and the Ph.D. degree in oceanography from the University of Delaware, Newark, in 1986. His Ph.D. dissertation focused on the dynamics of the Middle Atlantic Bight Shelfbreak Front.

He was with the Centre for Environmental Studies, University of Melbourne, where he worked for several years in environmental research and consulting. During 1986–2000, he was a Research Scientist with the Australian Institute of Marine Science, Townsville, where he conducted physical oceanographic and remote sensing studies of mesoscale circulation within the northern Australian marginal seas. Since 2001, he has been an Oceanographer with the Ocean Sciences Branch, Naval Research Laboratory, Stennis Space Center, MS. His research interests include microwave remote sensing of sea surface salinity, mesoscale circulation, and coastal ocean dynamics.

Dr. Burrage is a member of the American Meteorological Society, the Oceanography Society, and the American Geophysical Union.

Joel Wesson received the B.A. degree in physics from Swarthmore College, Swarthmore, PA, in 1982 and the Ph.D. degree in physical oceanography from the University of Washington, Seattle, in 1991.

From 1992 to 1995, he did postdoctoral work at McGill University, Montreal, QC, Canada, where he studied small-scale mixing processes in the Gulf of St. Lawrence as part of a JGOFS experiment. From 1995 to 2000, he was with Neptune Sciences Inc., Slidell, LA, where he primarily developed instruments for microbubble measurements in the coastal and surf zones in association with NRL. Since 2000, he has been with the Ocean Sciences Branch, Naval Research Laboratory, Stennis Space Center, MS, developing and deploying STARRS in a variety of locations and applications. His research interests include oceanographic instrument design and calibration, turbulence, internal waves, near-surface ocean physics, and salinity remote sensing.

Jerry Miller received the B.S. degree in marine science from the University of South Carolina, Columbia, in 1978, the M.S. degree in oceanography from the University of Rhode Island, Kingston, in 1982, and the Ph.D. degree in meteorology and physical oceanography from the University of Miami, Coral Gables, FL, in 1992.

He has since worked in academic, private consulting, and government laboratories. He is currently the Technical Director and Director of Research of the Consortium for Oceanographic Research and Education, Washington, DC. His research interests include coastal remote sensing, estuarine and coastal processes, and numerical modeling of coastal environments.